

A parallax distance to 3C 273 through spectroastrometry and reverberation mapping

Jian-Min Wang^{1,2,3}, Yu-Yang Songsheng^{1,2}, Yan-Rong Li¹, Pu Du¹ and Zhi-Xiang Zhang⁴

¹*Key Laboratory for Particle Astrophysics, Institute of High Energy Physics, Chinese Academy of Sciences, 19B Yuquan Road, Beijing 100049, China*

²*School of Astronomy and Space Science, University of Chinese Academy of Sciences, 19A Yuquan Road, Beijing 100049, China*

³*National Astronomical Observatories of China, Chinese Academy of Sciences, 20A Datun Road, Beijing 100020, China*

⁴*Department of Astronomy, Xiamen University, Xiamen, Fujian 361005, China*

Distance measurements for extragalactic objects are a fundamental problem in astronomy^{1,2} and cosmology^{3,4}. In the era of precision cosmology, we urgently need better measurements of cosmological distances to observationally test the increasing H_0 tension of the Hubble constant measured from different tools^{5–7}. Using spectroastrometry⁸, GRAVITY at The Very Large Telescope Interferometer successfully revealed the structure, kinematics and angular sizes of the broad-line region (BLR) of 3C 273 with an unprecedentedly high spatial resolution⁹. Fortunately, reverberation mapping (RM)¹⁰ of active galactic nuclei (AGNs) reliably provides linear sizes of their BLRs¹¹. Here we report a joint analysis of spectroastrometry and RM observations to measure AGN distances. We apply this analysis to 3C 273 observed by both GRAVITY⁹ and an RM campaign¹², and find an angular distance of $551.5^{+97.3}_{-78.7}$ Mpc and $H_0 = 71.5^{+11.9}_{-10.6}$ km s^{−1} Mpc^{−1}. Advantages of the analysis are 1) its pure geometrical measurements and 2) it simultaneously yields mass of the central black hole in the BLR. Moreover, we can conveniently repeat measurements of selected AGNs to efficiently reduce the statistical and systematic errors. Future observations of a reasonably sized sample (~ 30 AGNs) will provide distances of the AGNs and hence a new way of measuring H_0 with a high precision ($\lesssim 3\%$) to test the H_0 tension.

GRAVITY observations through spectroastrometry (SA) sensitively detect the angular struc-

ture of the BLR in a direction perpendicular to line-of-sight (LOS) whereas RM observations are more sensitive along the direction of the sight. A joint analysis of SA and RM observations of AGNs (hereafter SARM) can thus directly measure absolute angular distances (D_A). AGN emission lines arise from the photoionization of clouds by the central energy source^{15–17}. An assembly of ionized clouds orbiting around the central black hole with mass (M_\bullet), in which emission lines are broadened by the Doppler motion in the black hole gravity, is the well-known paradigm of the BLR. The SA measures the wavelength dependence of the photocentre of an object so that it provides information on the spatial structure of the object on scales much smaller than the diffraction limit¹⁸. For an interferometer with a baseline \mathbf{B} , a non-resolved source with a global angular size smaller than its resolution limit λ/B has the interferometric phase

$$\phi_*(\lambda, \lambda_r) = -2\pi \mathbf{u} \cdot [\boldsymbol{\epsilon}(\lambda) - \boldsymbol{\epsilon}(\lambda_r)], \quad (1)$$

where $\mathbf{u} = \mathbf{B}/\lambda$ is the spatial frequency, $\boldsymbol{\epsilon}$ is the photocentre of the source at wavelength λ and λ_r is the wavelength of a reference channel. Here the bold letters are vectors. We use an established approach^{19,20} to calculate differential phase curves (see also the Methods for details) for the angular sizes of the BLR if the BLR geometry is given for general cases. 3C 273, the first quasar discovered²¹, has a redshift of $z = 0.158$ and a K -band magnitude $K \approx 10.0$ (both from the NASA Extragalactic Database). GRAVITY successfully measured the differential phase curves (ϕ_*) of 3C 273 in July 2017, January, March, and May 2018⁹. The spectral resolution of GRAVITY is $\lambda/\Delta\lambda \approx 500$, which is good enough to constrain some parameters of the BLR from the observed Paschen α (hereafter Pa α) line. The present analysis is based on GRAVITY data.

As a consequence of photoionization, the broad emission lines respond to variations of the ionizing continuum with delays (usually the optical 5100Å continuum is used as a proxy). It has been observationally demonstrated that the RM technique measures the time lags of the lines with respect to the continuum and provides absolute sizes of the BLRs¹¹. 3C 273 is known as a blazar with a powerful jet²², but it has a prominent big blue bump dominating from optical to soft X-rays over the non-thermal emissions of the jet²³. The varying continuum is contaminated sometimes to some degrees by the jet's emission, but the prominent big blue bump emission dominates to govern H β reverberation most of the time. A 10-yr RM campaign of 3C 273 has been conducted through joint observations on the Bok 2.3m telescope at Steward Observatory, University of Arizona, and

the Lijiang 2.4m telescope in Yunnan Observatory, Chinese Academy of Sciences¹². The campaign using the Bok telescope started from March 2008 and the Lijiang telescope from December 2016 to May 2018. We have 296 spectra with a mean cadence of 7.4 days for the entire campaign. One comparison star was simultaneously observed in a long slit with 3C 273 and used for flux calibrations. This method generates high-quality light curves (LCs), with the $H\beta$ flux having a typical error at a $\sim 2\%$ level and the continuum at $\sim 1\%$. Details of the campaign and data reduction can be found in Ref.¹², from which this joint analysis takes the data.

Reverberation of broad emission lines delivers the linear sizes of the emitting regions while spectroastrometry probes their angular sizes, however, their geometrical sizes remain open without a reliable physical model of the regions, as they are usually explained as a kind of emissivity-averaged sizes or mean centers of λ -wavelength photons, respectively. We have to specify a BLR model for the joint analysis when we combine GRAVITY and RM data. Many efforts have been made to model the RM data of ~ 40 mapped AGNs in details through Markov Chain Monte Carlo simulations^{24,25}, offering empirical formulations of spatial distributions of the BLR clouds for the present joint analysis. We follow the approach described in Ref.^{24–26} for RM^{1D} modeling (see details in the Methods), but we take the simplest version of the current model by keeping necessary parameters, which are listed in Table 1. Here the roles of individual parameters in GRAVITY and RM data are also highlighted for the necessity of the joint analysis of GRAVITY and RM data. It is important to note that the joint analysis can simultaneously generate the distances and the central black hole masses of AGNs.

Modeling of RM data shows that the radial structure is described by a shifted Γ -distribution²⁶. The distance of BLR clouds from the SMBH is computed by $r = R_S + \mathcal{F}R_{\text{BLR}} + \Gamma_0\beta^2(1 - \mathcal{F})R_{\text{BLR}}$, where $R_S = 2GM_\bullet/c^2$ is the Schwarzschild radius, G is the gravitational constant, c is the speed of light, R_{BLR} is the mean radius, $\mathcal{F} = R_{\text{in}}/R_{\text{BLR}}$ is the fraction of the inner to the mean radius, and β is the shape parameter. Here $\Gamma_0 = p(x|\beta^{-2}, 1)$ is a random number drawn from a Γ -distribution $p(x|\alpha, x_0) = x^{\alpha-1} \exp(-x/x_0)/x_0^\alpha \Gamma(\alpha)$, where x_0 is a scale factor, $\alpha = \beta^{-2}$, and $\Gamma(\alpha)$ is the Γ -function. Such a radial distribution of BLR clouds is convenient for calculations and naturally covers several simple cases²⁶. On the other hand, multiple campaigns of several

AGNs show Keplerian rotation of the BLR clouds around the central black hole (see the Methods for details of the references). Moreover, this is also directly supported by the differential phase curves⁹ of 3C 273 which is also in agreement with the velocity-resolved delays¹². In this paper, we employ a Keplerian disc with an opening angle as the BLR model in 3C 273 for this joint analysis (see Supplementary Figure 1).

The joint analysis employs three datasets, which are 1) the long term RM data; 2) the differential phase curves; 3) the Pa α line profiles. The analysis can be conducted by maximizing the posterior probability distributions of the model parameters for the SARM data. We assume that the probability distributions for the measurement values of LCs, profiles and differential phase curves are Gaussian and uncorrelated. Accordingly, we generate their corresponding probabilities for fitting observational points of each dataset, which are $P_i^{f_\ell}$ for flux variations of H β line, $P_{i,j}^\phi$ for differential phase curves and $P_j^{F_\ell}$ for profiles of the Pa α line, respectively (given in the Methods). The joint likelihood function can be expressed by productions of the three probabilities,

$$P(\mathcal{D}|\Theta) = \prod_{i=1}^{N_{\text{RM}}} P_i^{f_\ell} \times \prod_{i=1}^{N_G} \prod_{j=1}^{N_\lambda} P_{i,j}^\phi \times \prod_{j=1}^{N_\lambda} P_j^{F_\ell}, \quad (2)$$

where \mathcal{D} represents the measured data, Θ represents all the model parameters. N_{RM} is number of RM observations, N_G is the number of GRAVITY observations (all the baselines) and N_λ is the corresponding number of wavelength bins. In light of Bayes' theorem, the posterior probability distribution for Θ is given by $P(\Theta|\mathcal{D}) = P(\Theta)P(\mathcal{D}|\Theta)/P(\mathcal{D})$, where $P(\Theta)$ is the prior distribution of the model parameters and $P(\mathcal{D})$ is a normalization factor.

In the Methods section, we show evidence for jet contamination of the observed continuum giving rise to trending effects before 2012 (see details in Ref.²⁷). Only the RM data after 2012 are thus taken into account in the joint analysis. The best-fittings to the SARM data are shown in Figure 1, , and the projection of probability density distributions are shown in Figure 2 for the three key parameters (R_{BLR} , M_\bullet , D_A). See Supplementary Figures 2 and 3 for the fittings of whole differential phase curves and projection of probability density distributions of the complete parameters. The median value and 1σ error bar for each parameter are also given there and listed in Table 1. Some parameters have values similar to those in Ref.⁹ within error bars, or different within rea-

sonable ranges. The present joint analysis generates an angular distance of $D_A = 551.5^{+97.3}_{-78.7}$ Mpc with a relative statistical error of $|\Delta D_A|/D_A \approx 0.16$ on average. This is a very encouraging accuracy for the joint analysis of the first SARM data, demonstrating the power of the present analysis as a feasible tool for measuring extragalactic distances. The SARM measurements as a geometrical method avoid various calibrations and corrections used in the popular measurements through Cepheid variable stars⁵ and type Ia supernovae (SNIa)^{13,14}, such as extinction corrections in both tools, necessary calibrations through the standardization and cosmic ladders in the latter.

Systematic errors of results in the joint analysis are mainly governed by three factors. As the first step of the SARM approach, we use the simplest model of the BLR to simultaneously fit GRAVITY data and RM LCs, namely, for one dimension fitting (2D model will include $H\beta$ profile and its variations; see Methods for more explanations). Since $\text{Pa}\alpha$ and $H\beta$ lines are both from $n = 4$ energy level to $n = 3, 2$, respectively, in principle, GRAVITY-measured $\text{Pa}\alpha$ regions should share the same regions with $H\beta$ line measured by RM. For the current case of 3C 273, however, they show small difference of the sizes ($\sim 13\%$) likely due to optical depths of the two lines in light of their profile width (see the Methods for details). Fortunately, the SARM analysis can completely avoid this problem if observations are for the same line, i.e., mapping $\text{Pa}\alpha$ in near infrared bands (such an RM campaign is actually in planning). Second, lengths of GRAVITY observations and RM campaigns are quite different and they measure the variable part and entire regions, respectively. This may give rise to differences measured by the two observations, however, we can conveniently justify this by comparing the RMS and mean spectra. We found that the two spectra of 3C 273 are similar in widths and shapes¹², implying that GRAVITY-measured regions are about identical to the RM-measured ones. Moreover, the dynamical timescale of the BLR is much longer than the length of our RM campaigns. The two conditions guarantee the validity of the joint analysis, and such a kind of systematic errors can be minimized. Third, non-disc like geometry or radial motion of BLR clouds could result in systematic errors in the analysis. In practice, fortunately, the velocity-resolved delays or its 2D delay maps from the maximum entropy method²⁸ provide key information to justify deviation of geometry and kinematics of the BLR from the simplest model, such as a disc-like geometry of the BLR with Keplerian rotation in 3C 273 supported by both velocity-resolved delays¹² and interferometric data⁹. In principle, all these

factors can be maximally avoided or at least observationally tested to reliably get systematic errors of measurements (see details of observational strategies in the Methods).

We can measure the Hubble constant H_0 through the SARM-based distance of 3C 273. Employing the $z - D_A$ relation¹, we have $H_0 = 71.5^{+11.9}_{-10.6} \text{ km s}^{-1} \text{ Mpc}^{-1}$ for a cosmology of $\Omega_M = 0.315$ and $\Omega_\Lambda = 0.685$ determined by the Planck CMB measurements⁶ (but H_0 very weakly depends on Ω_M and Ω_Λ for the current case). Considering the current accuracy of distance measurements of 3C 273 (this is mainly controlled by the error bars of the DFC measured by GRAVITY, which can be improved significantly in future observations), we have uncertainties of H_0 given by $|\Delta H_0|/H_0 = |\Delta D_A|/D_A \lesssim 3 N_{30}^{-1/2}$ per cent for a AGN sample of a reasonable size, where $N_{30} = N/30$ is the number of AGNs. A selection is done for K -band brighter than $\lesssim 11.5\text{mag}$ in the Supplementary Information (the $\sim 13\%$ uncertainties are not included since it can be in principle eliminated). Such a precision is enlightening for a test of the current H_0 -tension⁷. Targets of a future SARM project should be focused on AGNs with smooth and symmetric broad emission-line profiles in order to reduce systematic errors (or GRAVITY⁺ as a next generation of GRAVITY is designed for fainter targets in the near future, making target selection much easier). Advantages of the SARM-based measurements are obvious. First, the distance measurements are geometrical for H_0 . Though the SARM-based measurements depend on physical models, they can be observationally tested in advance. Second, SARM targets can be easily selected from existing AGN catalogs (and can be more distant than Cepheids and SNIa). Repeat measurements (invoking multiple campaigns of 2-4m class telescopes to simultaneously monitor the targets) allow us to test and greatly reduce systematic error bars. Third, the number of targets spatially distributed over the sky allows us to obtain high precision measurements of the $z - D_A$ relation for different directions in order to test the potential anisotropy of the accelerating expansion of the Universe²⁹ and advance the understanding of cosmological physics³⁰.

1. Peacock, J. A. *Cosmological Physics* (Cambridge Univ. Press, 1999).
2. de Grijs, R., & Cartwright, S. *An Introduction to Distance Measurement in Astronomy* (Wiley Online Library, 2011).
3. Freedman, W. L. & Madore, B. F. The Hubble constant. *Annu. Rev. Astron. Astrophys.* **48**,

673-710 (2010).

4. Weinberg, D. H., Mortonson, M. J., Eisenstein, D. J., Hirata, C., Riess, A. G. & Rozo, E. Observational probes of cosmic acceleration. *Phys. Rep.* **530**, 87-255 (2013).
5. Freedman, W. L. Cosmology at a crossroads. *Nature Astron.* **1**, 121 (2017).
6. Planck Collaboration, Aghanim, N., et al. Planck 2018 results. VI. Cosmological parameters. arXiv:1807.06209, 1-72 (2018).
7. Riess, A. G., Casertano, S., Yuan, W., Macri, L. M. & Scolnic, D. Large Magellanic cloud Cepheid standards provide a 1% foundation for the determination of the Hubble constant and stronger evidence for physics beyond Λ CDM. *Astrophys. J.* **876**, 85 (2019).
8. Gravity Collaboration, Abuter, R., et al. First light for GRAVITY: Phase referencing optical interferometry for the Very Large Telescope Interferometer. *Astron. Astrophys.* **602**, A94 (2017).
9. Gravity Collaboration, Sturm, E., et al. Spatially resolved rotation of the broad-line region of a quasar at sub-parsec scale. *Nature* **563**, 657-660 (2018).
10. Blandford, R. D. & McKee, C. F. Reverberation mapping of the emission line regions of Seyfert galaxies and quasars. *Astrophys. J.* **255**, 419-439 (1982).
11. Peterson, B. M. Reverberation mapping of active galactic nuclei. *Pub. Astron. Soc. Pac.* **105**, 247-268 (1993)
12. Zhang, Z.-X., et al. Kinematics of the broad-line region of 3C 273 from a 10 yr reverberation mapping campaign. *Astrophys. J.* **876**, 49 (2019).
13. Riess, A. G., et al. Observational evidence from supernovae for an accelerating Universe and a cosmological constant. *Astron. J.* **116**, 1009-1038 (1998).
14. Perlmutter, S., et al. Measurements of Ω and Λ from 42 high-redshift supernovae. *Astrophys. J.* **517**, 565-586 (1999).

15. Osterbrock, D. E., & Mathews, W. G. Emission-line regions of active galaxies and QSOs. *Annu. Rev. Astron. Astrophys.* **24**, 171-203 (1986).
16. Osterbrock, D. E. *Astrophysics of Gaseous Nebulae and Active Galactic Nuclei* (University Science Books, 1989).
17. Ho, L. C. Nuclear activity in nearby galaxies. *Annu. Rev. Astron. Astrophys.* **46**, 475-539 (2008).
18. Bailey, J. A. Spectroastrometry: a new approach to astronomy on small spatial scales. *Proc. SPIE* **3355**, Optical Astronomical Instrumentation, ed. S. D'Odorico, 932-939 (1998).
19. Petrov, R. G., et al. in European Southern Observatory Conference and Workshop Proceedings **39**, 435-443 (1992).
20. Rakshit, S., Petrov, R. G., Meilland, A., & Hönig, S. F. Differential interferometry of QSO broad-line regions - I. Improving the reverberation mapping model fits and black hole mass estimates. *Mon. Not. R. Astron. Soc.* **447**, 2420-2436 (2015).
21. Schmidt, M. 3C 273: a star-like object with large red-shift. *Nature* **197**, 1040-1040 (1963).
22. Courvoisier, T. J. L. The bright quasar 3C 273. *Astron. Astrophys. Rev.* **9**, 1-32 (1998).
23. Walter, R., et al. Simultaneous observations of Seyfert 1 galaxies with *IUE*, *ROSAT* and *GINGA*. *Astron. Astrophys.* **285**, 119-131 (1994).
24. Pancoast, A., Brewer, B. J., & Treu, T. Geometric and dynamical models of reverberation mapping data. *Astrophys. J.* **730**, 139-153 (2011).
25. Li, Y.-R., Wang, J.-M., Ho, L. C., Du, P., & Bai, J.-M. A Bayesian approach to estimate the size and structure of the broad-line region in AGNs using reverberation mapping data. *Astrophys. J.* **779**, 110 (2013).
26. Pancoast, A., Brewer, B. J., & Treu, T. Modelling reverberation mapping data - I. Improved geometric and dynamical models and comparison with cross-correlation results. *Mon. Not. R. Astron. Soc.* **445**, 3055-3072 (2014).

27. Li, Y.-R., et al. Untangling optical emissions of the jet and accretion disk in the flat-spectrum radio quasar 3C 273 with reverberation mapping data, *Astrophys. J.*(submitted), arXiv:1909.04511 (2019).
28. Horne, K., Welsh, W. F. & Peterson, B. M. Echo mapping of broad $H\beta$ emission in NGC 5548, *Astrophys. J. Letters* **367**, 5-8 (1991).
29. Cai, R.-G., Ma, Y.-Z., Tang, B. & Tuo, Z. L. Constraining the anisotropic expansion of the Universe. *Phys. Rev. D* **87**, 123522 (2013).
30. Weinberg, S. *Cosmology* (Oxford University Press, New York 2008).

Table 1: Parameters used in the BLR model and the SARM results of 3C 273

Parameters	meanings	GRAVITY	RM ^{1D}	Joint analysis	Prior ranges
\mathcal{F}	fractional inner radius of the BLR	\checkmark (0.23 ± 0.08)	\checkmark	$0.49^{+0.12}_{-0.20}$	[0, 1]
β	radial distribution of BLR clouds	\checkmark (1.4 ± 0.2)	\checkmark	$1.09^{+0.91}_{-0.40}$	[0, 4]
$\theta_{\text{opn}}(^{\circ})$	half opening angle of the BLR	\checkmark (45^{+9}_{-6})	\checkmark	$39.96^{+4.01}_{-3.72}$	[0, 90]
$i_0(^{\circ})$	inclination angle of the BLR	\checkmark (12 ± 2)	\checkmark	$8.41^{+0.99}_{-0.91}$	[0, 90]
PA($^{\circ}$)	position angles	\checkmark (210^{+6}_{-9})		$210.99^{+3.67}_{-4.63}$	[0, 520]
$R_{\text{BLR}}(\text{lt})$	averaged linear sizes		\checkmark	$184.17^{+16.77}_{-8.57}$	[1, 10 ³]
$M_{\bullet}(10^8 M_{\odot})$	supermassive black hole mass	2.6 ± 1.1		$5.78^{+1.11}_{-0.88}$	[10 ⁻² , 10]
$D_{\text{A}}(\text{Mpc})$	absolute angular distance	550 (assumed)		$551.50^{+97.31}_{-78.71}$	[10, 10 ⁴]
$\xi_{\text{BLR}}(\mu\text{as})$	averaged angular sizes	\checkmark (46 ± 10)		$59.70^{+8.72}_{-10.31}$	
$\zeta(10^{-2})$	dimensionless velocity parameter	\checkmark (1.01 ± 0.22)		$1.34^{+0.12}_{-0.06}$	

Notes: “ \checkmark ” means that the parameter can be determined by GRAVITY or RM data. Numbers in brackets behind “ \checkmark ” are median values with uncertainties of 90% from fittings of GRAVITY data⁹ for a convenient comparison. Values determined by the joint analysis are medians of the posterior distributions with uncertainties of 68% confidence ranges. RM^{1D}: one-dimensional reverberation mapping (RM), in which only flux variations of broad emission lines are fitted. $\xi_{\text{BLR}} = R_{\text{BLR}}/D_{\text{A}}$ (the angular sizes) and $\zeta = (GM_{\bullet}/R_{\text{BLR}})^{1/2}c^{-1}$ are reduced quantities for the fitting.

Acknowledgements We are grateful to three anonymous referees for useful reports improving this paper. We acknowledge the support by National Key R&D Program of China through grant - 2016YFA0400701, by NSFC through grants NSFC-11991050, -11873048, -11833008, -11573026, and by Grant No. QYZDJ-SSW-SLH007 from the Key Research Program of Frontier Sciences, CAS, by the Strategic Priority Research Program of the Chinese Academy of Sciences grant No.XDB23010400. E. Sturm is thanked for useful information of GRAVITY and the future GRAVITY⁺ capabilities. JMW is grateful to M. Brotherton for careful reading the manuscript and useful discussions, to Bo-Wei Jiang, Dong-Wei Bao, Wei-Jian Guo and Sha-Sha Li who helped for the target selections.

Author Contributions JMW conceived this project and wrote the paper. YYS, YRL and JMW made all calculations. ZXZ and PD made observations and perform data reduction. JMW, ZXZ and PD selected targets of the future SARM projects. All the authors discussed the contents of the paper.

Correspondence Correspondence and requests for materials should be addressed to Jian-Min Wang (email: wangjm@ihep.ac.cn). Jian-Min Wang: <https://orcid.org/0000-0001-9449-9268>

Competing Interests The authors declare that they have no competing financial interests.

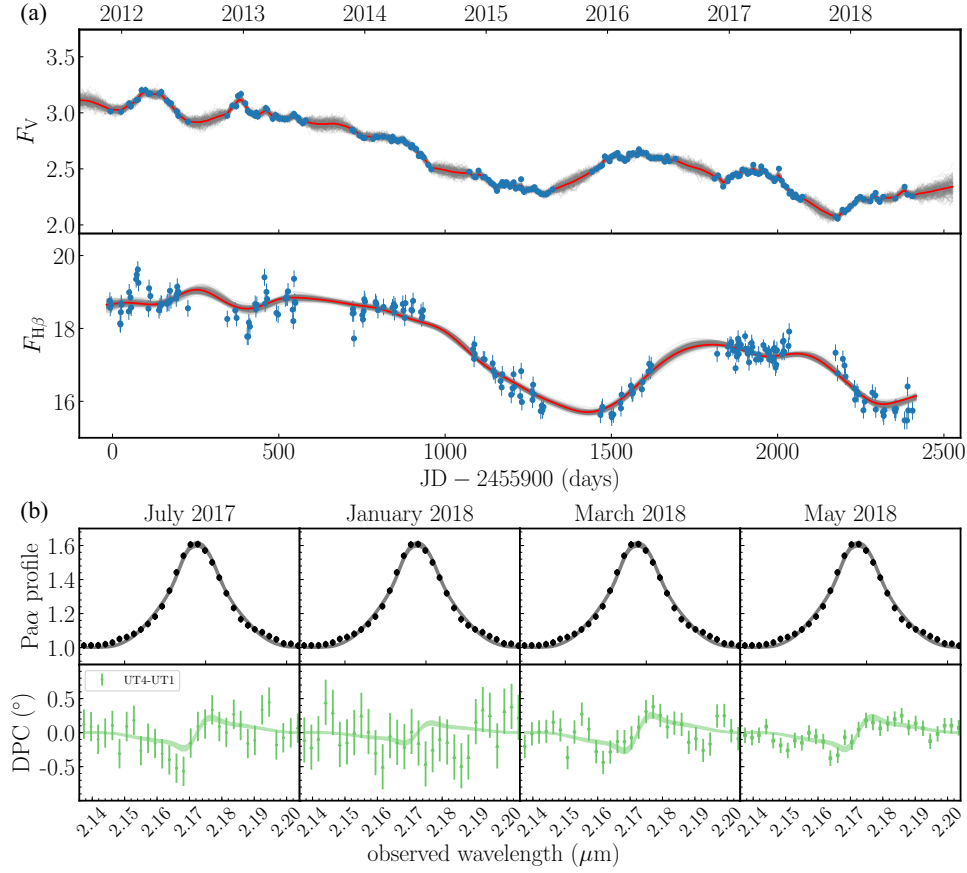


Figure 1 | Joint fittings of RM and GRAVITY observations. Panel *a*: one-dimensional fitting of the RM data since 2012 (avoiding contaminations of the relativistic jet, see details in Methods) through the BLR model. Blue points are data points with 1σ error bars; red lines are the best fitting results of LCs; gray ones are the results using 200 groups of model parameters randomly drawn from their probability distribution. The $H\beta$ fluxes are in units of $10^{-13} \text{ erg s}^{-1} \text{ cm}^{-2}$, and F_V in $10^{-14} \text{ erg s}^{-1} \text{ cm}^{-2} \text{ \AA}^{-1}$ converted from V -band magnitudes. The scatter of the $H\beta$ LC around the beginning of 2012, 2013 significantly contributes to $\chi^2 = 1.61$, which is relatively larger than that of GRAVITY data. Panel *b*: Fittings of the differential phase curves (DPC; green color points) of the baseline UT4-1 and $\text{Pa}\alpha$ line profiles (black points; $\chi^2 = 1.33$) as an example, and the complete fittings of all baselines are given in Methods. All the data points are with 1σ error bars; thick lines are the best fitting through the model with values of parameters given in Table 1; translucent thin lines are fitting results using 200 groups of model parameters randomly drawn from their probability distribution.

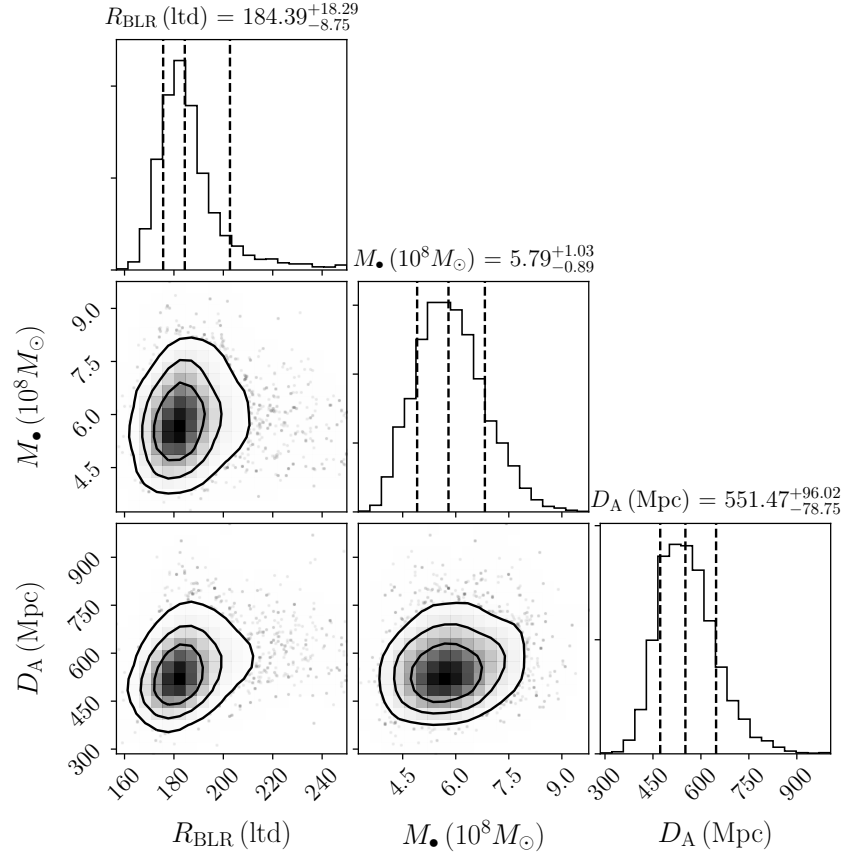


Figure 2 | Results of black hole mass and distances. Probability density distributions of three key parameters of the BLR and angular distances based on the joint analysis. The best values of the parameters are given on the tops of panels. Error bars are quoted at 1σ level, which are given by each distributions. The dashed lines in the one-dimensional distributions are the 16%, 50% and 84% quantiles, and contours are at 1σ , 1.5σ and 2σ , respectively.

Methods

Spectroastrometry. “Differential Speckle Interferometry” as the progenitor of the spectroastrometry was first suggested by J. M. Becker³¹ and its feasibility was demonstrated by R. Petrov¹⁹. We follow the description of interferometry in Ref.³² (but see also Ref.²⁰ for more extensive discussions). Spectroastrometry is a powerful tool of high spatial resolution. Given the surface brightness distribution of the regions, we have

$$\epsilon(\lambda) = \frac{\int \alpha \mathcal{O}(\alpha, \lambda) d^2\alpha}{\int \mathcal{O}(\alpha, \lambda) d^2\alpha}, \quad (3)$$

where $\mathcal{O}(\alpha, \lambda) = \mathcal{O}_\ell + \mathcal{O}_c$ is the surface brightness distribution of the source contributed by the BLR and continuum regions, respectively, and α is the angular displacement on the celestial sphere. Given the geometry and kinematics of a BLR, its \mathcal{O}_ℓ can be calculated for one broad emission line with the observed central wavelength λ_{cen} through

$$\mathcal{O}_\ell = \int \frac{\Xi_r F_c}{4\pi r^2} f(\mathbf{r}, \mathbf{V}) \delta(\alpha - \alpha') \delta(\lambda - \lambda') d^3\mathbf{r} d^3\mathbf{V}, \quad (4)$$

where $\lambda' = \lambda_{\text{cen}} \gamma_0 (1 + \mathbf{V} \cdot \mathbf{n}_{\text{obs}}/c) (1 - R_S/r)^{-1/2}$ includes gravitational shifts due to the central black hole, $\gamma_0 = (1 - V^2/c^2)^{-1/2}$ is the Lorentz factor, $\alpha' = [\mathbf{r} - (\mathbf{r} \cdot \mathbf{n}_{\text{obs}}) \mathbf{n}_{\text{obs}}] / D_A$, \mathbf{r} is the displacement to the central BH, Ξ_r is the reprocessing coefficient at position \mathbf{r} , $f(\mathbf{r}, \mathbf{V})$ is the velocity distribution of the clouds at that point, F_c is ionizing fluxes received by an observer, and $\mathbf{n}_{\text{obs}} = (0, \sin i_0, \cos i_0)$ is the unit vector pointing from the observer to the source. Introducing the fraction of the emission line to total (ℓ_λ), we have

$$\epsilon(\lambda) = \ell_\lambda \epsilon_\ell(\lambda), \quad (5)$$

where

$$\epsilon_\ell(\lambda) = \frac{\int \mathbf{r} \mathcal{O}_\ell d^2\alpha}{\int \mathcal{O}_\ell d^2\alpha}, \quad \ell_\lambda = \frac{F_\ell(\lambda)}{F_{\text{tot}}(\lambda)}, \quad F_\ell(\lambda) = \int \mathcal{O}_\ell d^2\alpha, \quad F_{\text{tot}}(\lambda) = F_\ell(\lambda) + F_c(\lambda).$$

Inserting Equations (5), (4) and (3) into (1), we can obtain phase curves. Since $B/\lambda \sim 100\text{m}/2.2\mu\text{m}$ and $\epsilon \sim 100\mu\text{as}$, ϕ_* -amplitudes are expected to be at a level of a few degrees for spatial resolution of compact objects. If the BLR model is specified, the spectroastrometric technique is able to efficiently improve the spatial resolution.

Reverberation mapping. AGNs and quasars are radiating with huge power and their spectra are prominently characterized by broad emission lines from NIR, optical to ultraviolet bands^{15–17}. The standard model of AGNs is accretion onto supermassive black holes (SMBHs) located in galactic centers producing powerful radiation³³. Emission lines from the photoionized gas are broadened by fast motions under the gravitational potential of the SMBHs and appear with a full width at half maximum (FWHM) spanning from $\sim 10^3$ to a few 10^4 km s^{-1} . According to energy conservation, the covering factor of the BLR clouds is about 10%, representing a fraction of reprocessing energy released by the accretion. As a natural consequence of photoionization, the emission lines will follow variations of the continuum, but with a delay denoted as τ_{BLR} . This delayed response is known as the reverberation of the BLR¹¹. Considering that the recombination timescale $\tau_{\text{rec}} \approx (n_e \alpha_B)^{-1} \approx 0.1 n_{10}^{-1} \text{ hr}$ is much shorter than τ_{BLR} , the delays of the emission lines represent the linear dimension of the emission line regions, where $n_{10} = n_e / 10^{10} \text{ cm}^{-3}$ is electron density of clouds and α_B is the case B recombination coefficient¹⁶.

RM observations measure the LCs of broad emission lines and continuum, and then allow us to investigate the temporal relation between the lines and the continuum for the BLR geometry and kinematics¹¹. Echo of emission lines to the continuum was suggested earlier³⁴, but observation campaigns began to measure it since 1980s. Nowadays, RM technique is regarded as the most powerful tool of measuring the central black hole mass³⁵ in studies of the so-called coevolution of SMBHs and galaxies³⁶. There are ~ 100 AGNs with robust $\text{H}\beta$ RM measurements (summarized in Ref.³⁷), this number is expected to dramatically increase contributed by several RM groups over the word in near future. In practice, τ_{BLR} can be easily measured from the simple cross-correlation function, however, its exact meaning can only be specified through modeling the BLR.

Parameterized BLR. The understanding of BLRs has been advanced much after great efforts of RM campaigns for about 100 AGNs during the last several decades^{38–41}. It has been found that, except for optical Fe II-strong AGNs^{41,42}, BLR sizes follow a well-established $R - L$ relation^{40,41} agreeing with the consequence of photoionization of isotropic ionizing sources. These Fe II-strong AGNs⁴¹ are mostly super-Eddington objects powered by slim accretion discs^{43,45,46}, breaking the assumption of isotropic ionizing sources made in the explanation of $\text{H}\beta$ line reverberation⁴⁶. Self-shadowing effects due to the puffed-up inner part of slim disks greatly obscure illuminations of

the BLR so that $H\beta$ lags are significantly shortened^{41,46}. For Fe II-weak AGNs, they are likely powered by geometrically thin accretion discs and can be well approximated as isotropic sources. Secondly, a disc-like BLR has been generally found in many broad-line Seyfert 1 galaxies from velocity-resolved delay maps^{40,47–50}, even in some narrow-line Seyfert 1 galaxies⁴⁹. Moreover, the differential phase curves of the $\text{Pa}\alpha$ line in 3C 273 directly show evidence for a Keplerian rotation of flattened disc as the BLR. Third, there is growing evidence for Keplerian rotation of the BLR clouds through multiple campaigns of several AGNs, such as, NGC 5548, NGC 3783, 3C 390.3 and NGC 7469⁵¹, stratified radial structure of the BLR according to the ionization energy of ions in NGC 5548⁵², or vertical structure of the BLR (see Figure 24 in Ref.⁵³). Additionally, the angle between the direction of orbital angular momentum and the Z -axis is uniformly distributed over $[0, \theta_{\text{opn}}]$, which is used in BLR modeling⁹. As the zero-order approximation of the present scheme, we simply assume that the BLR clouds are orbiting with Keplerian velocity around the central black hole in this paper. In such a characterized BLR, emission line profiles are usually symmetric. See Supplementary Figure 1 for the BLR geometry.

With the goal of illustrating a new scheme to determine distances, we employ a stream lined model of the BLR, rather than a comprehensive BLR model (with about ~ 20 parameters) pursuing fine fitting of the observational data as done in Ref.^{24–26,54,55}. The BLR model could include more components in the future if GRAVITY data is significantly improved.

We point out that the “clouds” used in this paper can be generally understood as elements of the BLR if it is a kind of fluid. These clouds could be supplied by the central black hole tidal capture of clumps from torus⁵⁶ or winds from accretion disc⁵⁷. The former model keeps a quasi-stationary state of the BLR whereas some clouds switch to the accretion disc of the black hole.

RM^{1D} modeling. Detailed descriptions of RM^{1D} modeling of the BLR are given by Ref.^{25,54}. Here we briefly summarize the necessary formulations for the reader’s convenience. In order to interpolate and extrapolate the sampled LC of the varying continuum, we use the damped random walk (DRW) model to describe the continuum variations^{58,59}. For a time series of \mathbf{y} , the measured data can be expressed by $\mathbf{y} = \mathbf{s} + \mathbf{n} + \mathbf{E}q$, where \mathbf{s} is the variation signal that is described by the DRW model, \mathbf{n} is the measurement errors, q is the mean values of the series, and \mathbf{E} is a vector

with all unity elements. The covariance function of the DRW model is given by

$$S(t_1, t_2) = \sigma_d^2 \exp\left(-\frac{|t_1 - t_2|}{\tau_d}\right), \quad (6)$$

for any two points at times t_1 and t_2 , where σ_d is the long-term standard deviation of the variations and τ_d is the typical timescale of the variations⁵⁸. Supposing that both \mathbf{s} and \mathbf{n} are Gaussian and unrelated^{25,54}, the best estimate of q is given by

$$\hat{q} = \frac{\mathbf{E}^T \mathbf{C}^{-1} \mathbf{y}}{\mathbf{E}^T \mathbf{C}^{-1} \mathbf{E}}, \quad (7)$$

where the superscript “ T ” denotes the transposition, $\mathbf{C} = \mathbf{S} + \mathbf{N}$, \mathbf{S} and \mathbf{N} are the covariance matrix of the signal \mathbf{s} and noise. Using Bayes’ theorem, we can recover the damped random walk process to determine the best values of σ_d and τ_d for a given set of the series. The most probable estimate of the variation signal \mathbf{s} at any time t_* is given by

$$\hat{\mathbf{s}} = \mathbf{S}^T \mathbf{C}^{-1} (\mathbf{y} - \mathbf{E} \hat{q}). \quad (8)$$

A typical realization for the continuum LC is⁵⁴

$$f_c = (\mathbf{u}_s + \hat{\mathbf{s}}) + \mathbf{E}(u_q - \hat{q}), \quad (9)$$

where \mathbf{u}_s follows a Gaussian process with a zero mean and covariance of $\mathbf{Q} = [\mathbf{S}^{-1} + \mathbf{N}^{-1}]^{-1}$, and u_q follows a Gaussian process with a zero mean and covariance of $(\mathbf{E}^T \mathbf{C}^{-1} \mathbf{E})^{-1}$. We treat \mathbf{u}_s and u_q as free parameters, which are further constrained by the LC data of the emission line.

All calculations are done using the coordinates shown in Supplementary Figure 1. Given the BLR geometry and kinematics, we can calculate the response of the entire BLR to the varying continuum in order to fit the observed data. The time-dependent fluxes of the broad emission line can be calculated by summing up the reprocessing emissions from all the BLR clouds as

$$f_\ell(t) = \int d\mathbf{r} dt' \frac{\Xi_r f_c(t')}{4\pi r^2} n(\mathbf{r}) \delta(t' - t + \tau) \quad (10)$$

where $\tau = (r - \mathbf{r} \cdot \mathbf{n}_{\text{obs}})/c$, Ξ_r is the reprocessing coefficient and $n(\mathbf{r})$ is the number density of the clouds. Given the BLR model, Equations (9,10) are used to fit the observed LCs denoted as the RM^{1D} analysis.

Observational data and de-trending. We note that the varying continuum has a long decreasing trend, but $H\beta$ LC does not have the same trend¹² (also see Supplementary Figures 4 and 5). It has been suggested that de-trending is an efficient way to improve the RM analysis of long-term secular variability of continuum^{51,60}. In the present scheme of fittings, we take a linear form of de-trending as $f_c \propto k_c(t - t_0)$ for the continuum LCs, where k_c is determined by the joint analysis.

Contamination. In Supplementary Figure 4, we show the γ -ray LC monitored by the LAT of the *Fermi* satellite (<https://fermi.gsfc.nasa.gov/ssc/data/access/>). The ≥ 30 GeV emission must be generated by the most inner part of the jet⁶¹, and thus contamination could be tested by γ -rays. The *Fermi* monitoring campaign is continuous without season gaps, allowing us to test the long-term trend. We generate the γ -ray LC according to the *Fermi* user's Guider (see also the γ -ray LC in Ref.⁶²). It is obvious that there is a giant γ -ray flare in the second half year of 2009 and first months of 2010, and the flare has a long tail lasting to the end of 2011. It is not the goal of the present paper to make a detailed comparison between the γ -ray and V -band LCs, but it is quite obvious that the flare significantly contributes to the observed optical continuum. It is also clear that the response of the broad $H\beta$ line to the optical continuum is weak. The jet contamination has been investigated²⁷ through analysis of multiple long-term light curves from radio to optical band, as well as polarization. It is clear that the long term trend of 5100Å continuum is due to the jet contaminations. See details in this reference.

Weak response of the broad $H\beta$ line. Entire LCs are shown by Supplementary Figure 5a, 5b and 5c. With the de-trended continuum LC, we obtained a lag of $\tau_{\text{BLR}} = 146 \pm 8$ days¹². We shifted the $H\beta$ LC backward by the $(1 + z)\tau_{\text{BLR}}$ and multiplied $F_{H\beta}$ by a reasonable factor for a compare with the de-trended continuum in Supplementary Figure 5d. It is clear that the response of $H\beta$ is weak before 2012. One plausible reason is that the optical continuum is contaminated (UV is less significantly) by the jet located outside the BLR, but the BLR has no response to this continuum component. We only focus on the linear response at the zero-order of the model, rather than non-linear responses of the BLR clouds in this paper.

Fittings. Clouds are randomized to distribute along a given orbit. We use this prescription of cloud distribution for the calculation of transfer functions, line profiles, and differential phase curves.

Special and general relativistic effects are included. We take the priors of the BLR parameters in sufficiently wide ranges in order to guarantee the unique solutions of the model. Ranges of parameters are provided in Table 1. The priors of $(\mathcal{F}, \beta, \theta_{\text{opn}}, i_0, \text{PA})$ are uniform over the given intervals, while those of $(R_{\text{BLR}}, M_{\bullet}, D_A)$ are uniform in log scale. The cosmological dilation factor of $(1+z)$ has been included in generating LC to fit observations of 3C 273 in the BLR modeling. Using the Diffusive Nested Sampling⁶³, we obtain a total of 5000 samples for all model parameters. We generate probabilities in Equation (2), $P_i^{f_\ell}$ for $\text{H}\beta$ reverberation, $P_{i,j}^\phi$ for differential phase curves and $P_j^{F_\ell}$ for profiles of the $\text{Pa}\alpha$ line,

$$P_i^{f_\ell} = \frac{1}{\sqrt{2\pi\sigma_\ell^2}} \exp \left\{ -\frac{[f_{\ell,i}^{\text{obs}} - f_{\ell,i}^{\text{mod}}(f_{\text{c,obs}}|\Theta)]^2}{2\sigma_\ell^2} \right\}, \quad (11)$$

$$P_{i,j}^\phi = \frac{1}{\sqrt{2\pi\sigma_{\phi_{ij}}^2}} \exp \left\{ -\frac{[\phi_{i,j}^{\text{obs}} - \phi_{i,j}^{\text{mod}}(\Theta)]^2}{2\sigma_{\phi_{ij}}^2} \right\}, \quad (12)$$

$$P_j^{F_\ell} = \frac{1}{\sqrt{2\pi\sigma_F^2}} \exp \left\{ -\frac{[F_{\ell,j}^{\text{obs}} - F_{\ell,j}^{\text{mod}}(\Theta)]^2}{2\sigma_F^2} \right\}, \quad (13)$$

where $f_{\ell,i}^{\text{obs}}$, $F_{\ell,j}^{\text{obs}}$, and $\phi_{i,j}^{\text{obs}}$ are the observed line flux, line profile, and interferometric phase of the emission line with measurement uncertainties σ_ℓ , $\sigma_{\phi_{ij}}$, and σ_F , respectively, and $(f_{\ell,i}^{\text{mod}}, F_{\ell,j}^{\text{mod}}, \phi_{\ell,i}^{\text{mod}})$ are the corresponding predicted values from the BLR model.

The joint analysis of the SARM data shows the reduced $\chi_G^2 = 1.33$ for GRAVITY data and $\chi_{\text{RM}}^2 = 1.61$ for the RM data. The χ_{RM}^2 is a little bit higher than χ_G^2 , but note that this could be caused by a couple of points in the $\text{H}\beta$ LC significantly deviating from the model. Excluding these points, we find that the χ^2 will be greatly reduced. Considering the major goals of the present paper, we keep this fitting with the $\chi^2 = 1.61$ as resultant fittings. We found $k_c = (7.9 \pm 0.2) \times 10^{-5}$ from the joint fitting, which is consistent with the results in Ref.²⁷

We generated mock data to test the present scheme. Error bars of GRAVITY phase curves are set to be $\sim 25\%$ and RM data at the level of the 3C 273 campaign. We find that the generated parameters of the model from the mock data are in good agreement with the input within 10%.

This demonstrates that the present joint analysis is feasible for simultaneous determinations of distances and black hole mass of AGNs.

Quasars as cosmological probes. Quasars are the most luminous and long-lived celestial objects in the Universe. After their discovery, they were instantly suggested as probes for cosmology^{64–67} by arguing that some properties of quasars can serve as “standards”. However, these efforts were not successful because of poor understanding of quasar physics. Recently, interests in applications of quasars to cosmology have arisen again by selecting special individual objects or populations in light of their well-understood properties.

Direct measurements of distances through very long base interferometry (VLBI) observations of water masers in NGC 4258 ($z \approx 0.0015$)⁶⁸, and torus diameters through direct imaging observations of NGC 4151 ($z \approx 0.0033$)⁶⁹ have been suggested for cosmology, but these methods are limited either by the rare sources of water masers or the long period of NIR monitoring campaigns. Parallax of quasar BLR was suggested for measurements of distances^{72,73}, which needs an interferometer with a baseline of $\sim 100\text{km}$, but GRAVITY at The Very Large Telescope Interferometer (with baselines of only $\sim 100\text{m}$) employs spectroastrometry to efficiently reduce the required baseline for $10\mu\text{as}$ resolution. Super-Eddington accreting massive black holes (SEAMBHs over much wider ranges of redshifts) from their saturated luminosity^{41,43,44,46,74–76} were suggested for cosmology and show potential feasibilities of application to the high- z Universe⁷⁷. Moreover, the following relations have been also suggested for cosmology, such as the well-known $R-L$ relation of sub-Eddington AGNs^{78–80} or its improved version⁸¹, NIR continuum reverberation correlation⁸², X-ray variance versus luminosity⁸³, and the non-linear UV versus X-ray luminosity relation⁸⁴. Quasars as cosmological objects seem to be a promising tool to probe the Universe in future^{85,86}, but much work needs to be done for precision cosmology as a robust probe.

We would like to point out that all the methods mentioned above need calibrations of cosmic ladders except for the way of the VLBI water maser and NIR RM techniques. The application of the $R-L$ relation to cosmology has been initiated^{80,87,88}, but emission-line lags for high- z quasars are hard to measure because of the dilation factor of $(1+z)$. SEAMBHs as a new kind of cosmic ladders can be in principle extended to high- z quasars^{89,90} from the local scaling relation⁹¹.

Moreover, the present SARM analysis provides a direct method without the calibration issues of known cosmic ladders or extinction corrections. Future GRAVITY observations of low- z SEAMBHs will provide an efficient way of calibrating SEAMBHs into the high- z Universe. It is then expected to use AGNs for accurate measurements of distances from low- z to high- z Universe. Calibrations by different ladders are not necessary in the current approach.

As inquired by one of referees, we applied the simplest estimation of 3C 273 distances through torus image and NIR RM data. The angular size of its torus is $\Delta\theta_{\text{tor}} = 0.29 \text{ mas}$ is from Keck interferometer observations⁷⁰ and the linear size $\Delta R_{\text{tor}} \approx 1.0 \text{ lt-yr}$ from the long term K -band light curve and the optical-UV⁷¹. We have a distance of $D_A = \Delta R_{\text{tor}} / \Delta\theta_{\text{tor}} \approx 212 \text{ Mpc}$, which is smaller a factor of 2.6 than the present determination and the ΛCDM model, but it is still encouraging. We note that the K -band light curve has too poor cadences after 1995 to reliably determine ΔR_{tor} (see their Figure 2 in Ref.⁷¹), moreover, this estimation needs to be improved through the sophisticated scheme to obtain ΔR_{tor} and $\Delta\theta_{\text{tor}}$ for distances like in Ref.⁶⁹. It should be noted that NIR continuum RM campaigns are usually much longer than the $\text{H}\beta$ ones.

Uncertainties from the BLR model. Geometrical measurements of both GRAVITY and the RM data depend on the BLR model, which is assumed to be a geometrically thick disc with Keplerian rotation. More complicated structures and kinematics of the BLRs are possible, however, we should note that they can be observationally tested for systematic errors, which can be independently estimated from observational data of RM campaigns through comparing with mock data.

Differences compared with sole GRAVITY measurements. As shown in Table 1 and Supplementary Figure 3, some results from the SARM analysis are significantly different from that from analysis of sole GRAVITY data, however they seem to be reasonable. As shown by Equation (1), the phase curves are more sensitive to the BLR information projected to the baseline direction. RM of broad $\text{H}\beta$ line mainly delivers its information along LOS. With different sensitivities of GRAVITY and RM data on model parameters, the joint analysis gets benefits from that some degeneracies of parameters are broken by the simultaneous application of both databases and hence generates more robust results. For example, the SARM analysis yields $M_{\bullet} = 5.78_{-0.88}^{+1.11} \times 10^8 M_{\odot}$ with relative errors smaller than that of $M_{\bullet} = 2.6 \pm 1.1 \times 10^8 M_{\odot}$ from the pure SA analysis⁹ (we

noted a $\sim 2.0\sigma$ M_\bullet -tension here). The SARM-measured M_\bullet is also more reliable than the simple virial mass of black hole (M_{vir})¹². The reasons are obvious: M_{vir} depends on the virial factor, while the factor is determined by calibrating with $M_\bullet - \sigma$ relation⁹². Moreover, $\text{H}\beta$ lags (even its error bars are very small) generated by cross correlation analysis remain quite ambiguous in their exact physical meanings since the lags do not fully cover the regions corresponding to its $\text{H}\beta$ FWHM. Currently, the lags of broad emission lines are explained as an emissivity-averaged radius of the BLR, however, the geometric radius can be specified after fixing a physical model. Once given the BLR geometry and kinematics, a joint analysis of GRAVITY and RM data generates the BLR parameters of the best fittings for both independent datasets (GRAVITY and RM data) simultaneously. For 3C 273, both D_A and M_\bullet are quite robust [see the circle shapes of contours in Supplementary Figure 3 except for (β, \mathcal{F}) , $(R_{\text{BLR}}, \mathcal{F})$ and $(M_\bullet, \theta_{\text{opn}})$]. On the other hand, we expect SARM observations of more targets to better understand the differences between the SARM with others (such as the slight M_\bullet -tension).

Geometry and kinematics. Roughly speaking, symmetric profiles of broad emission lines form from axisymmetric discs. The characterized BLR model of a geometrically thick disc with Keplerian rotation can be observationally tested by repeating campaigns (conveniently in principle). Velocity-resolved delays independent of models, or the 2D delay maps obtained from maximum entropy method²⁸ can directly justify the BLR geometry by comparing them with the shapes of known geometries, such as inflows or outflows^{50,93}. Moreover, the Keplerian rotating disc follows a simple relation of $\tau_{\text{BLR}} \propto V_{\text{FWHM}}^{-2}$, as in NGC 5548 and others mentioned previously. It is thus feasible to estimate the uncertainties of BLR geometry and kinematics contributed to systematic error bars of the model parameters.

We should note that GRAVITY measured the $\text{Pa}\alpha$ line region whereas the 10-yr RM campaign observed the $\text{H}\beta$. A fully self-consistent scheme should employ the same line for GRAVITY and RM campaign, however, an RM campaign of near infrared emission lines is much harder than $\text{H}\beta$ line. As argued in the main text, we in principle expect that $\text{Pa}\alpha$ and $\text{H}\beta$ regions should be the same in the simplest model. However, V_{FWHM} of $\text{H}\beta$ and $\text{Pa}\alpha$ lines are slightly different, implying the two-line regions may mismatch due to different optical depths for $\text{H}\beta$ and $\text{Pa}\alpha$ photons. A simple estimation can be done by following. Supposing the averaged radius (R_0) of the BLR

with a difference ΔR for the two lines, we have $(R_0 + \Delta R)V_{\text{Pa}\alpha}^2 = (R_0 - \Delta R)V_{\text{H}\beta}^2$ from the assumption that the two-line regions are virialized, where $V_{\text{Pa}\alpha, \text{H}\beta}$ are FWHMs of their profiles. We obtain the relative difference of $\Delta R/R_0 = (q - 1)/(q + 1)$, where $q = (V_{\text{H}\beta}/V_{\text{Pa}\alpha})^2$. According to the long campaign of 3C 273, we have $V_{\text{H}\beta} \approx (3100 - 3300)\text{km s}^{-1}$ changing with luminosity¹² while $V_{\text{Pa}\alpha} \approx (2700 - 3000)\text{km s}^{-1}$ from GRAVITY⁹ and NASA Infrared Telescope Facility (IRTF) observation⁹⁴. Taking the averaged values of $V_{\text{Pa}\alpha, \text{H}\beta} \approx (2800, 3200)\text{km s}^{-1}$, we have $\Delta R/R_0 = 13\%$. This error bar is comparable to that of distance measurements, but it can be greatly eliminated in the RM^{2D} modeling. Additionally, statistics show that Pa α line shares the same region with H β line⁹⁵. Ideally, RM should monitor the same emission line with GRAVITY in order to reduce the potential differences between RM and GRAVITY detections. A NIR-RM campaign of monitoring Pa α of 3C 273 is then expected for this goal.

On the other hand, the current analysis of the RM^{1D}+GRAVITY can be extended to that of the RM^{2D}+GRAVITY through allowing for different but partially overlapped regions for the two lines, which includes information of variations of H β profiles in the analysis of RM data^{26,54}. In such a modeling scheme, the profile variations will be moderately sensitive to the vertical structure of the BLR. Since Pa α line share the partially same regions with the H β , we relax \mathcal{F} and R_{BLR} to cover the two regions for different profiles of the two lines. However, the two regions share the same geometry and kinematics, such as, the same θ_{opn} and kinematics. Moreover, parameters describing cloud properties, such as anisotropy of line emissions, will be included in the RM^{2D} modeling^{26,54,55}. Though new parameters are added in RM^{2D} modeling, there are about 300 profiles of H β spectra of 3C 273 available to set more constraints on the parameters, providing opportunities to have better measurements of black hole mass and distance. This is the major contents of a separate paper of the joint analysis of GRAVITY and RM^{2D} modeling BLR for distances.

Radiation pressure. Motion of BLR clouds could be affected by radiation pressure^{96,97}, which changes kinematics of the clouds. Considering that the pressure decreases with the square of the distance to the black hole (for the simplest version of the pressure), we can combine its effects into the gravitational potential so that we can get the effective mass of the black hole in such a case. The effective mass of the black hole could be slightly smaller than the present, but the distance to observers remains the same.

Dimensionless accretion rates of AGNs can be estimated by $\dot{\mathcal{M}}_{\bullet} = 20.1 (\ell_{44} / \cos i_0)^{3/2} M_7^{-2}$, where $\dot{\mathcal{M}}_{\bullet} = \dot{M}_{\bullet} / \dot{M}_{\text{Edd}}$, \dot{M}_{\bullet} and $\dot{M}_{\text{Edd}} = L_{\text{Edd}} / c^2$ are accretion rates of the black hole and Eddington rate, respectively, L_{Edd} is the Eddington luminosity, ℓ_{44} is the 5100Å luminosity in units of $10^{44} \text{ergs s}^{-1}$ and $M_7 = M_{\bullet} / 10^7 M_{\odot}$. The $\dot{\mathcal{M}}_{\bullet}$ is derived from the standard accretion disc model⁴⁵. Taking $\ell_{44} = 84.3$ from our RM campaign¹² and $M_7 = 57.8$ from the SARM analysis, we have $\dot{\mathcal{M}}_{\bullet} \approx 4.7$ in 3C 273, implying a slight super-Eddington accretor compared with others⁴¹. In such a case, the radiation pressure on cloud's motion is not serious for mass estimations⁹⁷. Actually, the pressure can be included in the joint analysis of MCM modeling for more accurate measurements of black hole masses (or effective mass), fortunately, distance determinations escape from its influence. We would point out that the SARM analysis provides the most accurate mass of black holes in type I AGNs so far, and we will include radiation pressure to improve SARM analysis further for discussions related with coevolution of SMBHs and their hosts.

BLR variations. BLRs are known to vary with luminosities, such as in NGC 5548 (Figures 6, 8, 13 in Ref.^{48,98,99}, respectively). Since GRAVITY observations only take a few hours, which are much shorter than durations of RM campaigns (denoted as Δt_{RM} which is usually from a few months to years), GRAVITY may detect the changing BLR at different epochs from the RM campaigns. This may be one origin of the systematic uncertainties. For 3C 273, its RM campaign is as long as 10yr whereas GRAVITY observations just took snaps over a few hours or so in the last two years. The timescale of BLR variation is roughly given by $\Delta t_{\text{BLR}} \approx R_{\text{BLR}} / V_{\text{FWHM}} = 42 \tau_{150} V_{3000}^{-1} \text{yr}$ for dynamical changes, where $\tau_{150} = \tau_{\text{BLR}} / 150 \text{days}$ and $V_{3000} = V_{\text{FWHM}} / 3000 \text{km s}^{-1}$. Considering $\Delta t_{\text{RM}} \ll \Delta t_{\text{BLR}}$, we think that the current SARM analysis of 3C 273 avoids potential variations of the BLR in last ten years (the ionization fronts are fast changing with luminosity as $\Delta R_{\text{BLR}} / R_{\text{BLR}} \approx 0.5 \Delta L_{5100} / L_{5100}$ and it is $\lesssim 7\%$ from Supplementary Figure 5). In order to avoid systematic errors from the BLR variations, we should do RM campaigns in the same period of GRAVITY observations in future SARM projects. It is fortunate that GRAVITY observations of 3C 273 was covered by our campaign, efficiently reducing this influence on the present results.

One question may be asked if the RM-measured BLR is the same with GRAVITY measured regions because RM only measures the variable parts of the BLR and GRAVITY does the entire. This problem can be justified by comparing the mean and the RMS spectra for differences. For 3C

273, fortunately, it is clear that the RMS shape is very similar to its mean spectrum as shown in Figure 2 in Ref.¹². On the contrary, if the RMS is very distinguished from the mean spectra, GRAVITY measured BLR may be very different from the RM parts making the SARM analysis elusive. In practice, GRAVITY observations can be scheduled once at the beginning and ending epochs to find if the BLR changes. This strategy of observations can avoid the mis-matched measurements between GRAVITY and RM.

Degrees of ordered motion. Spectroastrometry measures the mean centers of λ -photons from the BLR and thus depends on its angular momentum distributions, namely on the degree (\mathcal{R}_0) of ordered motion of the BLR clouds^{20,100,101}. Fully ordered motion of BLR clouds, $\mathcal{R}_0 = 1$, is presumed in Ref.⁹ about GRAVITY observations of 3C 273. In principle, \mathcal{R}_0 should be treated as a free parameter in fitting the DPCs of GRAVITY data, but it strongly degenerates with the BLR sizes. \mathcal{R}_0 could be estimated from the position angles of polarized spectra arising from scattering by hot electrons in the mid-plane^{102,103}. Building up the relation between \mathcal{R}_0 and position angles of the polarized spectra will be very helpful to understand the \mathcal{R}_0 parameter of BLR clouds, but we have to introduce more parameters describing the electron scattering zone. This is much beyond the scope of the present paper, but we will treat this problem separately.

Error budgets. Error sources are generally from several aspects discussed in previous sections in addition to the measurements of GRAVITY observations and RM campaigns (for ideal SARM observations, namely, focus on the same line). First, the degree of disordered motion could contribute uncertainties to the present analysis. This involves the formation of the BLR, either from disc winds⁵⁷ or tidally captured clumps from a dusty torus⁵⁶. We expect to test \mathcal{R}_0 through polarized spectra. Second, non-Keplerian kinematics and a non-disc BLR could be other sources of systematic errors. Fortunately, this can be evaluated by repeating RM campaigns of individual AGNs to demonstrate the sources through direct test of the relation between $\tau_{H\beta}$ – FWHM and velocity-resolved delay relation ($\tau_{H\beta} - V$) for the BLR geometry, where V is the velocity bin. Actually, the systematic errors can be efficiently alleviated through selecting targets with symmetric profiles of broad emission lines. Third, the quasi-simultaneous observations of GRAVITY and RM campaigns might imply different regions measured by the two tools. However, this could be avoided if the SARM observations can be performed under reasonable schedule of observations or

within a BLR dynamical timescale. Fourth, selection of radial and angular distributions of BLR clouds in the model is another source of systematic errors for both GRAVITY and RM data. In order to quantitatively issue the errors, we need to simulate models to show error bars. Detailed discussions on this problem are beyond the scope of this paper, but we leave it in a future work.

Finally, for individual 3C 273, some errors are from observations of the RM campaign. There are a few key valleys and peaks for the determinations of model parameters, however, they are in season gaps, such as the second half years of 2012, 2015, 2016, 2017. Accuracies of model parameters are then affected in the joint analysis. Actually, we continue the campaign with a goal of getting more diagnostic valleys and peaks in next few years.

Future SARM projects. Spectroastrometry and reverberation mapping must come together for excellent studies of AGN physics and cosmology, but also for close-binaries of supermassive black holes (CB-SMBHs)^{101,104} radiating nano-Hertz gravitational waves (to be detected by the Pulsar Timing Arrays¹⁰⁸). Only GRAVITY observations of 3C 273 have been reported so far⁹, but similar targets selected from existing catalogs are listed for future SARM project in the Supplementary Table 1. GRAVITY will install new grisms in October 2019 so that $K \approx 11.0 - 11.5$ targets can be observed as routine research of AGNs. We note most the targets with redshifts $z \lesssim 0.08$, in which only $\text{Br}\gamma$ line (is significantly fainter than $\text{Pa}\alpha$ line) could be detected by GRAVITY. Simulations for 3C 120 ($K = 10.78$, see Supplementary Table 1) showed very promising detections of the $\text{Br}\gamma$ line, which was given by a talk of M. R. Stock. It can be found from website of the workshop (<https://www.torus2018.org/TALKS/18.12.10-S3.3-Stock.pdf>). From page 15 of the talk's file, we find that $\text{Br}\gamma$ interferometric signals are strong enough for a joint analysis in the future. On the other hand, $\text{Br}\gamma$ line forms from a transition of electrons from $n = 7$ to 4. In such a context, we should understand differences of $\text{Br}\gamma$ and $\text{H}\beta$ line regions through CLOUDY and test results from the $\text{RM}^{2\text{D}}$ +GRAVITY modeling. we thus expect that the current GRAVITY observes the targets listed here in near future. Optical spectra of all the targets are given in Supplementary Figure 6. The targets actually cover three kinds of AGNs: 1) Fe II-strong objects; 2) candidates of CB-SMBHs appearing with $\text{H}\beta$ asymmetry; 3) Fe II-weak objects.

A brief strategy of the future SARM projects could be as outlined below. RM campaigns of

the targets are expected to perform: 1) reveal velocity-resolved delays for kinematics and geometry (with physical sizes); 2) construct 2-dimensional transfer functions for justifying CB-SMBH candidates; 3) show stability of the BLR from multiple campaigns, for the goal of establishing BLR properties including stability of their structures. This needs much work of 2m telescopes to prepare for GRAVITY observations. After then, GRAVITY observations provide differential phase curves for structure, kinematics and angular sizes of the BLR. On the other hand, RM of GRAVITY near-infrared emission lines will, in principle, provide fully self-consistent data for the joint analysis. In such a campaign, targets should be selected more carefully to avoid NIR absorptions of the atmosphere. The campaigns could be conducted through 4m-class telescopes. We outline three aspects below (but they are valid for RM campaigns of $H\beta$ line with different broad emission lines in NIR).

SARM observations are for scientific goals as followings. Targets will be spatially resolved by GRAVITY observations along with RM campaigns to explore signatures of flattened rotating disc, inflows, or outflows in BLR in order to study accretion process and formation of the BLR connecting with dusty torus⁵⁶. In particular, those of optical Fe II-strong AGNs (about 1/3 of PG quasars¹⁰⁹) usually have smaller BLRs compared with objects with the same luminosities (significantly downward deviating from the well-known $R - L$ relation)⁴¹, and most of them are super-Eddington accreting massive black holes (SEAMBHs). SARM-based measurements of SEAMBHs might reveal more details of BLR structure and kinematics as well as physics of super-Eddington accretion process. Moreover, super-Eddington accretion process as a key phase across cosmic time is a critical step toward fast growth of seed black holes to form SMBHs in high- z Universe^{110–113}. This is very compelling for the increasing large samples of DESI (Dark Energy Survey Instrument) to tackle growth and formation issues of the SMBHs. Third, SEAMBHs are suggested to be a new kind of cosmic candles for the high- z cosmology^{45,74,76}. SARM-based measurements of SEAMBHs will build up precision ladders approaching to high- z Universe.

With the unprecedented power of high-spatial resolutions, GRAVITY offers opportunity of spatially resolve CB-SMBHs. AGNs with asymmetric profiles have likely more complicated BLR structures, and some of them could be CB-SMBH candidates^{104,114}. A dedicated project of Monitoring AGNs with $H\beta$ Asymmetry (MAHA) is being conducted to construct 2-dimensional transfer

functions^{104–106} through the Wyoming Infrared Observatory 2.3m telescope¹¹⁵ for the CB-SMBHs of future GRAVITY observations. The MAHA project is expected to provide the most promising candidates of the CB-SMBHs for GRAVITY, and for a joint analysis of the SARM data¹⁰¹. We would like to point out that Ark 120, Mrk 704 and several others show interesting features of CB-SMBHs in their 2D transfer functions. They are good targets of GRAVITY observations with obvious signatures of differential phase curves¹⁰⁷ in near future. Moreover, it could be possible to measure orbital parameters (such as masses of component black holes, inclination and ellipticity of the orbits) by the joint analysis of SARM data in order to predict properties of low-frequency gravitational waves radiated by the CB-SMBHs.

Optical Fe II-weak AGNs are usually sub-Eddington accretors⁴¹. We select some of them with stable and flattened-Keplerian disc-like BLR guaranteeing physical conditions of the SARM targets to efficiently reduce systematic errors of distance measurements of AGNs. They are excellent targets of GRAVITY observations for cosmology outlined in this paper. Fortunately again, this can be done by RM campaigns using 2m telescopes. From Supplementary Table 1, we have about $N \approx (30, 50)$ targets with $K \lesssim (11.0, 11.5)$, respectively. This makes it feasible to establish a future SARM project for the H_0 -measurements, providing $\Delta H_0/H_0 \lesssim (3, 2)$ per cent, respectively, which are valid for a test of the current H_0 -tension. With one 4yr SRAM project for ~ 100 AGNs, we can achieve $\sim 1.5\%$. If the uncertainties ($\sim 13\%$ in 3C 273) are included, $N \approx 200$ could be necessary. However, in principle, this systematic errors can be alleviated by RM^{2D}+GRAVITY measurements, hence, the $N \approx 200$ should be significantly reduced. On the other hand, with capability of future interferometers in space (spatial resolution up to $\sim 1\mu\text{as}$ by the *SIM*-Lite for optical $\sim 20\text{mag}$ AGNs^{116,117}), we can accurately measure all information of the $H\beta$ line region (angular and linear sizes) in optical bands for low- z quasars so that this systematic errors completely vanish. The H_0 -measurements can be done with unprecedented precisions by an AGN sample much smaller than the present estimates. GRAVITY⁺ with much improved sensitivity¹¹⁸ is expected to explore high- z cosmology (i.e., the Hubble parameter) through the present SARM scheme. In this case, one needs to use larger telescope (e.g., 5m class) to monitor GRAVITY+ targets in order to avoid too long RM campaigns. It should be stressed again that this is geometric for high- z cosmology.

In a brief summary, the near future SEAMBH-, CB-SMBH-, and H_0 -SARM projects will significantly advance understanding of AGN physics, close-binaries of supermassive black holes for nano-Hertz gravitational waves, and precision cosmology, respectively. It is highly desired to perform the three feasible projects in a few years.

Data Availability. The data that support the plots within this paper and other findings of this study are available from the corresponding author upon reasonable request.

Code Availability. All the codes used in this paper are available from the corresponding author upon reasonable request.

31. Beckers, J. M. Differential speckle interferometry. *Optica Acta* **29**, 361-362 (1982).
32. Petrov, R. G. Differential Interferometry. in *NATO Advanced Science Institutes (ASI) Series C*, ed. D. M. Alloin & J. M. Mariotti **274**, 249 (1989).
33. Rees, M. J. Black hole models for active galactic nuclei. *Annu. Rev. Astron. Astrophys.* **22**, 471-506 (1984).
34. Bahcall, J. N., Kozlovsky, B.-Z., & Salpeter, E. E. On the time dependence of emission-line strengths from a photoionized nebula. *Astrophys. J.* **171**, 467-482 (1972).
35. Peterson, B. M. Measuring the masses of supermassive black holes. *Sp. Sci. Rev.* **183**, 253-275 (2014).
36. Ferrarese, L. & Ford, H. Supermassive black holes in galactic nuclei: past, present and future research. *Sp. Sci. Rev.* **116**, 523-624 (2005).
37. Kaspi, S. Studying the outskirts of reverberation mapped AGNs. *IAU Sym.* **324**, 219-222 (2017).
38. Peterson, B. M., et al. Optical continuum and emission-line variability of Seyfert 1 galaxies. *Astrophys. J.* **501**, 82-93 (1998).
39. Kaspi, S., et al. Reverberation measurements for 17 quasars and the size-mass-luminosity relations in active galactic nuclei. *Astrophys. J.* **533**, 631-649 (2000).

40. Bentz, M. C. et al. The low-luminosity end of the radius-luminosity relationship for active galactic nuclei. *Astrophys. J.* **767**, 149 (2013)
41. Du, P. et al. Supermassive black holes with high accretion rates in active galactic nuclei. IX. 10 new observations of reverberation mapping and shortened H β lags. *Astrophys. J.* **856**, 6 (2018).
42. Du, P. & Wang, J.-M. The radius-luminosity relationship depends on optical spectra in active galactic nuclei. *Astrophys. J.* **886**, 42 (2019).
43. Abramowicz, M. A., Czerny, B., Lasota, J. P., & Szuszkiewicz, E. Slim accretion disks. *Astrophys. J.* **332**, 646-658 (1988).
44. Wang, J.-M. & Zhou, H.-Y. Self-similar solution of optically thick advection-dominated flows. *Astrophys. J.* **516**, 420-424 (1999).
45. Wang, J.-M. et al. Supermassive black holes with high accretion rates in active galactic nuclei. II. The most luminous standard candles in the Universe. *Astrophys. J.* **793**, 108 (2014).
46. Wang, J.-M., Qiu, J., Du, P., & Ho, L. C. Self-shadowing effects of slim accretion disks in AGNs: the diverse appearance of the broad-line region. *Astrophys. J.* **797**, 65 (2014).
47. Grier, C. J. et al. The structure of the broad-line region in active galactic nuclei. I. Reconstructed velocity-delay maps. *Astrophys. J.* **764**, 47 (2013).
48. Lu, K.-X. et al. Reverberation mapping of the broad-line region in NGC 5548: Evidence for radiation pressure? *Astrophys. J.* **827**, 118 (2016).
49. Du, P. et al. Supermassive black holes with high accretion rates in active galactic nuclei. VI. Velocity-resolved reverberation mapping of the H β line. *Astrophys. J.* **820**, 27 (2016).
50. Xiao, M. et al. A high-quality velocity-delay map of the broad-line region in NGC 5548. *Astrophys. J.* **865**, L8 (2018).
51. Peterson, B. M. et al. Central masses and broad-line region sizes of active galactic nuclei. II. A homogeneous analysis of a large reverberation-mapping database. *Astrophys. J.* **613**, 682-699 (2004).

52. Peterson, B. M. & Wandel, A. Evidence for supermassive black holes in active galactic nuclei from emission-line reverberation. *Astrophys. J.* **540**, L13-L16 (2000).
53. Kollatschny, W., Ulbrich, K., Zetzl, M., Kaspi, S., & Haas, M. Broad-line region structure and kinematics in the radio galaxy 3C 120. *Astron. Astrophys.* **566**, A106 (2014).
54. Li, Y.-R. et al. Supermassive black holes with high accretion rates in active galactic nuclei. VIII. Structure of the broad-line region and mass of the central black hole in Mrk 142. *Astrophys. J.* **869**, 137 (2018).
55. Williams, et al. The Lick AGN Monitoring Project 2011: Dynamical modeling of the broad-line region. *Astrophys. J.* **866**, 75 (2018).
56. Wang, J.-M. et al. Tidally disrupted dusty clumps as the origin of broad emission lines in active galactic nuclei. *Nature Astron.* **1**, 775783 (2017).
57. Czerny, B., & Hryniewicz, K. The origin of the broad line region in active galactic nuclei. *Astron. Astrophys.* **525**, L8 (2011).
58. Kelly, B. C., Bechtold, J., & Siemiginowska, A. Are the variations in quasar optical flux driven by thermal fluctuations? *Astrophys. J.* **698**, 895-910 (2009).
59. Zu, Y., Kochanek, C. S., Kozłowski, S., & Udalski, A. Is quasar optical variability a damped random walk? *Astrophys. J.* **765**, 106(2013).
60. Welsh, W. F. On the reliability of cross-correlation function lag determinations in active galactic nuclei. *Pub. Astron. Soc. Pac.* **111**, 1347-1366 (1999).
61. Blandford, R. D., & Levinson, A. Pair cascades in extragalactic jets. I. γ -rays. *Astrophys. J.* **441**, 79-95 (1995).
62. Meyer, M., Scargle, J. D., & Blandford, R. D. Characterizing the γ -ray variability of the brightest flat spectrum radio quasars observed with the *Fermi*-LAT. *Astrophys. J.* **877**, 39 (2019).
63. Brewer, B. J., & Foreman-Mackey, D. DNest4: diffusive nested sampling in C⁺⁺ and Python. *J. of Statistical Software* **86**, 1-33 (2018).

64. Sandage, A. The existence of a major new constituent of the Universe: the quasi-stellar galaxies. *Astrophys. J.* **141**, 1560-1579 (1965).
65. Hoyle, F. Relation between the red-shifts of quasi-stellar objects and their radio and optical magnitudes. *Nature* **210**, 1346-1347 (1966).
66. Longair, M. S., & Scheuer, P. A. G. Red-shift magnitude relation for quasi-stellar objects. *Nature* **215**, 919-922 (1967).
67. Baldwin, J. A. Luminosity indicators in the spectra of quasi-stellar objects. *Astrophys. J.* **214**, 679-684 (1977).
68. Humphreys, E. M. L., Reid, M. J., Moran, J. M., Greenhill, L. J., & Argon, A. L. Toward a new geometric distance to the active galaxy NGC 4258. III. Final results and the Hubble constant. *Astrophys. J.* **775**, 13 (2013).
69. Hönig, S. F., Watson, D., Kishimoto, M., & Hjorth, J. A dust-parallax distance of 19 megaparsecs to the supermassive black hole in NGC 4151. *Nature* **515**, 528-530 (2014).
70. Kishimoto, M. et al. The innermost dusty structure in active galactic nuclei as probed by the Keck interferometer. *Astron. Astrophys.* **527**, 121 (2011).
71. Soldi, S. et al. The multiwavelength variability of 3C 273. *Astron. Astrophys.* **486**, 411-425 (2008).
72. Elvis, M. & Karovska, M. Quasar parallax: a method for determining direct geometrical distances to quasars. *Astrophys. J. Letters* **581**, 67-70 (2002).
73. Quercellini, C., Cabella, P., Amendola, L., Quartin, M., Balbi, A. Cosmic parallax as a probe of late time anisotropic expansion. *Phys. Rev. D* **80**, 3527 (2009).
74. Wang, J.-M., Du, P., Valls-Gabaud, D., Hu, C., & Netzer, H. Super-Eddington accreting massive black holes as long-lived cosmological standards. *Phys. Rev. Lett* **110**, 081301 (2013).
75. Du, P. et al. Supermassive black holes with high accretion rates in AGNs. I. First results from a new reverberation mapping campaign. *Astrophys. J.* **782**, 45 (2014).

76. Marziani, P., & Sulentic, J. W. Quasars and their emission lines as cosmological probes. *Mon. Not. R. Astron. Soc.* **442**, 1211-1229 (2014).
77. Cai, R.-G., Guo, Z.-K., Huang, Q.-G., & Yang, T. Super-Eddington accreting massive black holes explore high- z cosmology: Monte-Carlo simulations. *Phys. Rev. D* **97**, 123502 (2018).
78. Watson, D., Denney, K. D., Vestergaard, M., & Davis, T. M. A new cosmological distance measure using active galactic nuclei. *Astrophys. J.* **740**, L49 (2011).
79. Czerny, B., Hryniewicz, K., Maity, I., Schwarzenberg-Czerny, A., Życki, P. T., Bilicki, M. Towards equation of state of dark energy from quasar monitoring: reverberation strategy. *Astron. Astrophys.* **556**, A97 (2013).
80. King, A. L. et al. Simulations of the OzDES AGN reverberation mapping project. *Mon. Not. R. Astron. Soc.* **453**, 1701-1726 (2015)
81. Martínez-Aldama, M. L. et al. Can reverberation-measured quasars be used for cosmology? *Astrophys. J.* **883**, 170 (2019).
82. Yoshii, Y., Kobayashi, Y., Minezaki, T., Koshida, S., Peterson, B. A. A new method for measuring extragalactic distances. *Astrophys. J.* **784**, L11 (2014).
83. La Franca, F., Bianchi, S., Ponti, G., Branchini, E., & Matt, G. A new cosmological distance measure using active galactic nucleus X-Ray variability. *Astrophys. J.* **787**, L12 (2014).
84. Risaliti, G., & Lusso, E. Cosmological constraints from the Hubble diagram of quasars at high redshifts. *Nature Astron.* **3**, 272-277 (2019).
85. Czerny, B. et al. Astronomical distance determination in the space age secondary distance indicators. *Space Sci. Rev.* **214**, 32-100 (2018).
86. Marziani, P. et al. Quasars: from the physics of line formation to cosmology. *Atoms* **7**, 18-30 (2019).
87. Czerny, B. et al. Time delay measurement of Mg II line in CTS C30.10 with SALT. *Astrophys. J.* **880**, 46 (2019).

88. Hoormann, J. K. et al. C IV black hole mass measurements with the Australian Dark Energy Survey (OzDES). *Mon. Not. R. Astron. Soc.* **487**, 3650-3663 (2019).
89. Negrete, C. A. et al. Highly accreting quasars: The SDSS low-redshift catalog. *Astron. Astrophys.* **620**, A118 (2018).
90. Martínez-Aldama, M. L. et al. Extreme quasars at high redshift. *Astron. Astrophys.* **618**, A179 (2018).
91. Du, P., Wang, J.-M., Hu, C., Ho, L. C., Li, Y. R., Bai, J. M. The fundamental plane of the broad-line region in active galactic nuclei. *Astrophys. J.* **818**, L14 (2016).
92. Onken, C. A. et al. Supermassive black holes in active galactic nuclei. II. Calibration of the black hole mass-velocity dispersion relationship for active galactic nuclei. *Astrophys. J.* **615**, 645-651 (2004).
93. Welsh, W. F., & Horne, K. Echo images of broad-line regions in active galactic nuclei. *Astrophys. J.* **379**, 586-591 (1991).
94. Landt, H. et al The near-infrared broad emission line region of active galactic nuclei. I. The observations. *Astrophys. J. Supp.* **174**, 282-312 (2008).
95. Landt, H. et al. A near-infrared relationship for estimating black hole masses in active galactic nuclei. *Mon. Not. R. Astron. Soc.* **432**, 113-126 (2013).
96. Marconi, A. et al. The effect of radiation pressure on virial black hole mass estimates and the case of narrow-line Seyfert 1 galaxies. *Astrophys. J.* **678**, 693-700 (2008).
97. Netzer, H. & Marziani, P. The effect of radiation pressure on emission-line profiles and black hole mass determination in active galactic nuclei. *Astrophys. J.* **724**, 318-328 (2010).
98. Peterson, B. et al. Steps toward determination of the size and structure of the broad-line region in active galactic nuclei. XV. Long-term optical monitoring of NGC 5548. *Astrophys. J.* **510**, 659-668 (1999).
99. Pei, L. et al. Space telescope and optical reverberation mapping project. V. Optical spectroscopic campaign and emission-line analysis for NGC 5548. *Astrophys. J.* **837**, 131 (2017).

100. Stern, J., Hennawi, J. F., & Pott, J.-U. Spatially resolving the kinematics of the $\lesssim 100 \mu\text{s}$ quasar broad-line region using spectroastrometry. *Astrophys. J.* **804**, 57 (2015).
101. Songsheng, Y.-Y., Wang, J.-M., Li, Y.-R. & Du, P. The VLT interferometric measurements of active galactic nuclei: effects of angular momentum distributions of clouds in the broad-line region. *Astrophys. J.* **883**, 184 (2019).
102. Smith, J. E., Robinson, A., Young, S., Axon, D. J., & Corbett, E. A. Equatorial scattering and the structure of the broad-line region in Seyfert nuclei: evidence for a rotating disc. *Mon. Not. R. Astron. Soc.* **359**, 846-864 (2005).
103. Songsheng, Y.-Y., & Wang, J.-M. Measuring black hole mass of type I active galactic nuclei by spectropolarimetry. *Mon. Not. R. Astron. Soc.* **473**, L1-L5 (2018).
104. Wang, J.-M., Songsheng, Y.-Y., Li, Y.-R. & Yu, Z. Kinematic signatures of reverberation mapping of close binaries of supermassive black holes in active galactic nuclei. *Astrophys. J.* **862**, 171 (2018).
105. Songsheng, Y.-Y., Wang, J.-M., Li, Y.-R. & Ho, L. C. Kinematic signatures of reverberation mapping of close binaries of supermassive black holes in active galactic nuclei. II. Atals of 2D-transfer functions. *Astrophys. J.* submitted (2019).
106. Kovacevic, A., Wang, J.-M. & Popovic, L. Kinematic signatures of reverberation mapping of close binaries of supermassive black holes in active galactic nuclei. III. The case of elliptical orbits. arXiv:191008709, (2019).
107. Songsheng, Y.-Y., Wang, J.-M., Li, Y.-R. & Du, P. Differential interferometric signatures of close binaries of supermassive black holes in active galactic nuclei. *Astrophys. J.* **881**, 140 (2019).
108. Burke-Spolaor, S. et al. The astrophysics of nanohertz gravitational waves. *Astron. Astrophys. Rev.* **27**, 5-82 (2019).
109. Boroson, T. A., & Green, R. F. The emission-line properties of low-redshift quasi-stellar objects. *Astrophys. J. Supp.* **80**, 109-135 (1992).

110. Volonteri, M. & Rees, M. J. Rapid growth of high-redshift black holes. *Astrophys. J.* **633**, 624-629 (2005).
111. Wang, J.-M., Chen, Y.-M. & Zhang, F. Feedback limits rapid growth of seed black holes at high redshift. *Astrophys. J.* **637**, L85-L88 (2006).
112. Milosavljević, M., Bromm, V., Couch, S. M. & Oh, S. P. Accretion onto “seed” black holes in the first galaxies. *Astrophys. J.* **698**, 766-780 (2009).
113. Regan, J. A. et al. Super-Eddington accretion and feedback from the first massive seed black holes. *Mon. Not. R. Astron. Soc.* **486**, 3892-3906 (2019).
114. Nguyen, K., Bogdanović, T., Runnoe, J. C., Jessie C., Eracleous, M., Sigurdsson, S., Boroson, T. Emission signatures from sub-parsec binary supermassive black holes. II. Effect of accretion disk wind on broad emission lines. *Astrophys. J.* **870**, 16 (2019).
115. Du, P. et al. Monitoring AGNs with $H\beta$ Asymmetry. I. First results: velocity-resolved reverberation mapping. *Astrophys. J.* **869**, 142 (2018).
116. Unwin, S. C., et al. Taking the measure of the Universe: precision astrometry with *SIM PlanetQuest*. *Pub. Astron. Soc. Pac.* **120**, 38-88 (2008).
117. Ding, F. & Croft, R. A. C. Future dark energy constraints from measurements of quasar parallax: *Gaia*, *SIM* and beyond. *Mon. Not. R. Astron. Soc.* **397**, 1739-1747 (2009).
118. Widmann, F. et al. Improving GRAVITY towards observations of faint targets. *Proc. the SPIE* **10701**, 6 (2018).

Supplementary Information

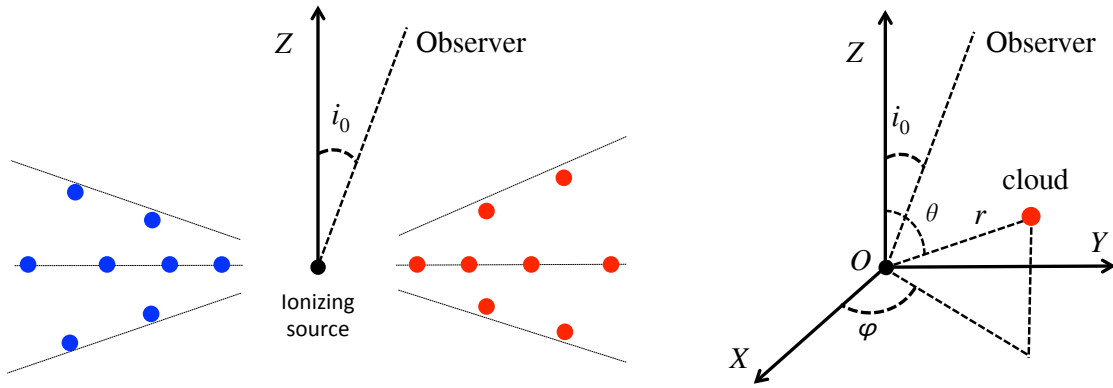
In this Section, we provide all figures used in Methods, target selection and target list including name, coordinates and spectra for future SARM observations.

The Figures are

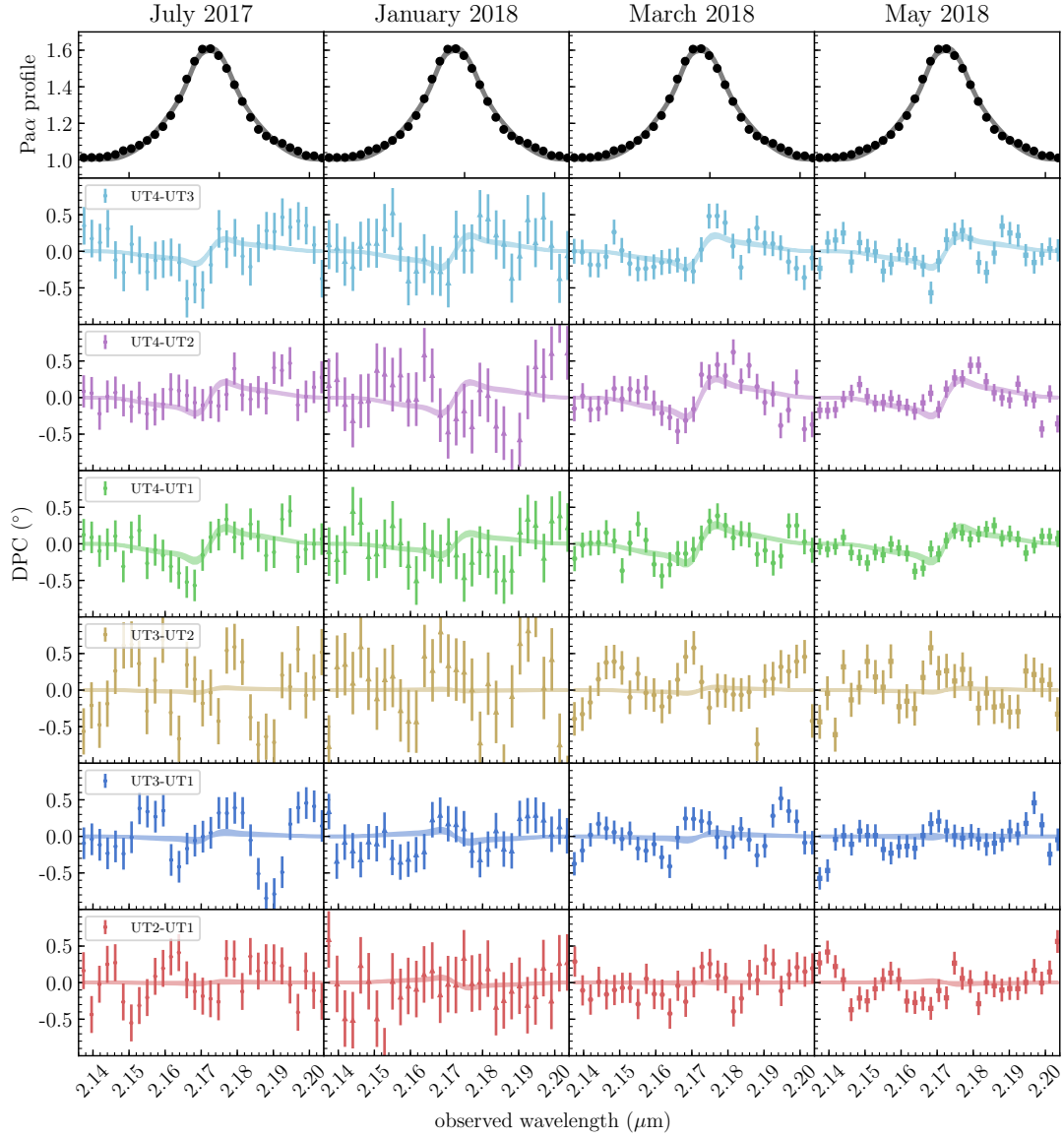
- Carton of the broad-line regions to illustrate the current model used in this paper (Supplementary Figure 1).
- Fittings of the differential phase curves observed by GRAVITY (Supplementary Figure 2).
- Results of probability distributions of physical parameters in the fittings (Supplementary Figure 3).
- Light curves of γ -rays and V -band (Supplementary Figure 4).
- Light curves of optical continuum and $H\beta$ line since 2009 (Supplementary Figure 5).

SARM target selection We selected targets from existing catalogs of AGNs. They are from the 2dF¹, 6dF² (also available from <http://vizier.u-strasbg.fr/viz-bin/VizieR>), the Veron Catalog of Quasars and Active Galactic Nuclei³, the Hamburg/ESO Survey⁴, and the Quasar Catalog of Sloan Digital Sky Surveys⁵. Two criteria are used for selection: 1) coordinates $\text{Dec.} \leq 20^\circ$ for GRAVITY of the VLTI (we assume that 2m telescopes are available for the SARM project in both southern and northern hemispheres); 2) K -band magnitudes $K < 11.5$ for the GRAVITY (private communications with E. Sturm). Supplementary Table 2 lists the targets with necessary information including $H\beta$ lags if measured, or estimated from the normal $R - L$ relation⁶, angular sizes of the BLR according to the standard Λ CDM model ($H_0 = 67 \text{ km s}^{-1} \text{ Mpc}^{-1}$, $\Omega_\Lambda = 0.315$ and $\Omega_M = 0.685$). All targets listed here are type I AGNs. Future observations of spectroscopic surveys of 4MOST (<https://www.4most.eu/cms/>) will greatly increase numbers of targets for the SARM project. Supplementary Table 2 is useful both for GRAVITY observations and RM campaigns for RM community over the world to make the SARM analysis in future. We also

provide one single epoch of all the targets in Supplementary Figure 6, but it should be noted that profiles of the $H\beta$ line change generally.

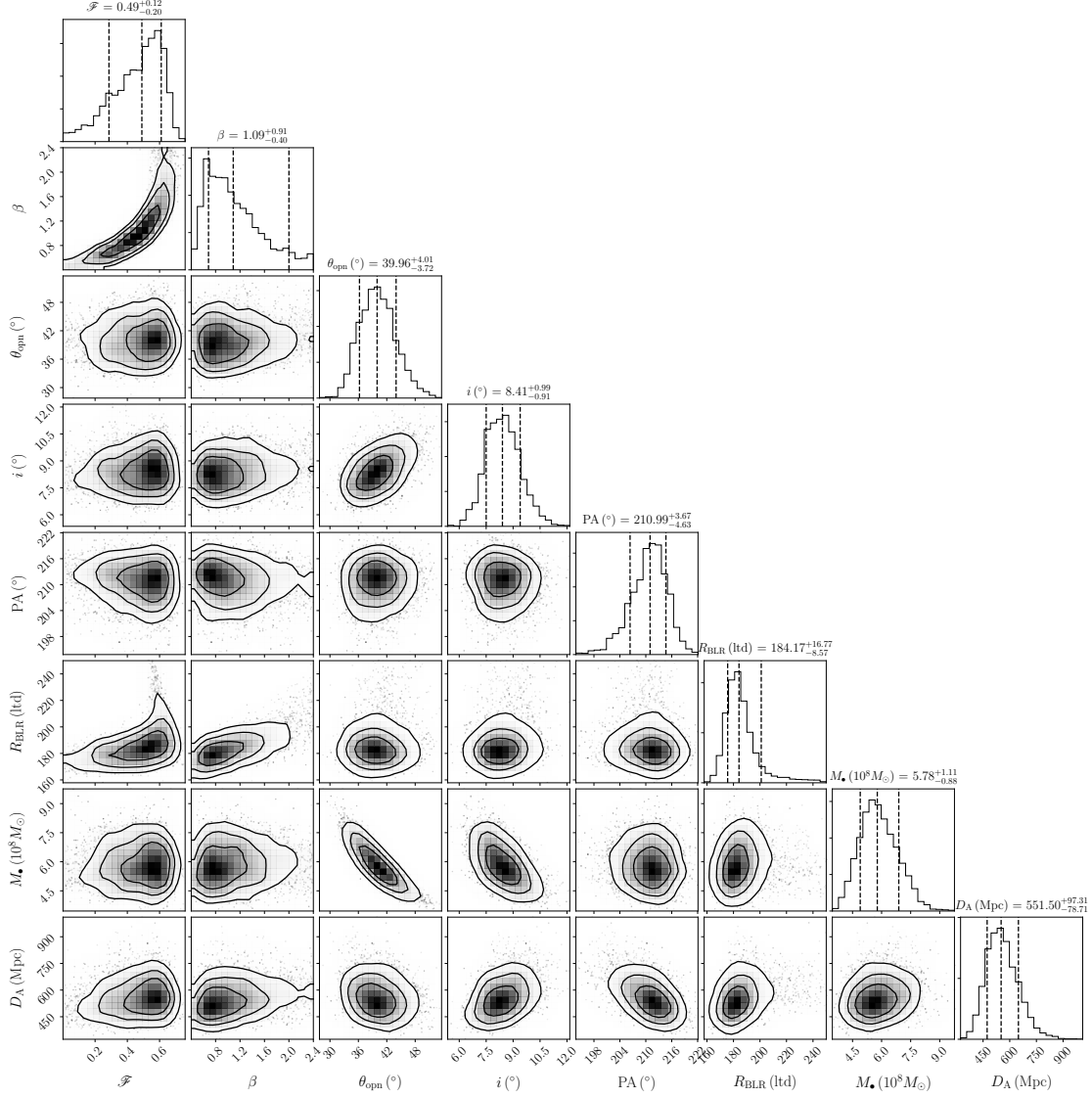


Supplementary Figure 1. Structure, geometry and kinematics of the simplest BLR in AGNs. It is characterized by a flattened disc with opening angle of θ_{opn} . The left panel is a cartoon illustration of the BLR. Clouds are presumed to be optically thin and are orbiting around the central black hole with Keplerian velocity. The blue and red clouds are approaching and receding to observers, respectively. A remote observer has an inclination of i_0 located in the $O - YZ$ plane. The right panel is the coordinate system we used. Here r is the distance of the cloud to the central SMBH, while θ and ϕ are polar and azimuthal angle of the cloud respectively.



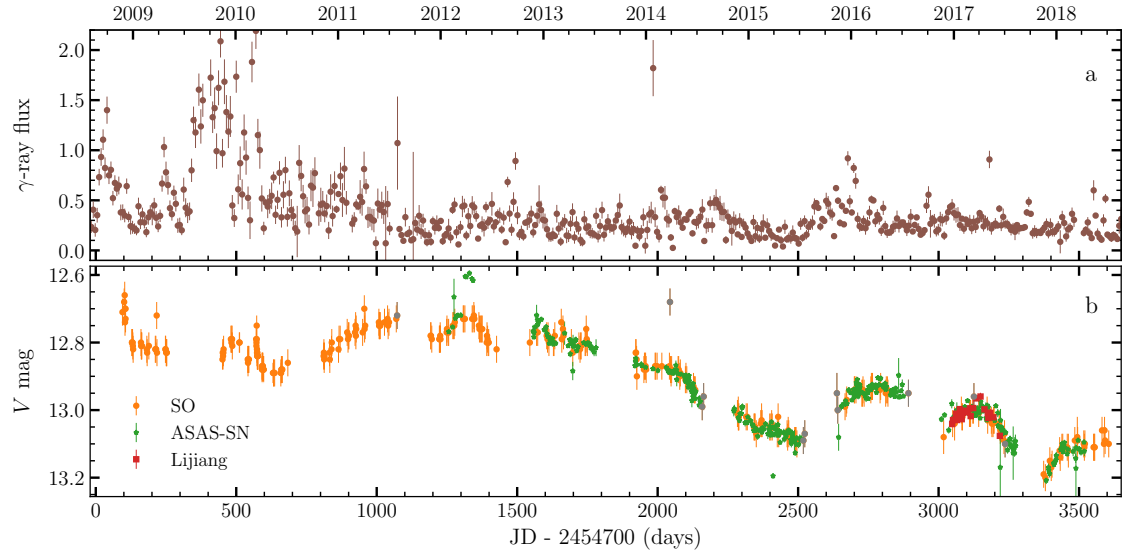
Supplementary Figure 2. Fittings of the DPCs from the 24 baseline interferometric data (the reduced $\chi^2 = 1.33$).

Different colors indicates DPCs from different telescope pairs. The first rows are Pa α line profiles taken from averaged profiles of the four epochs observed. The DPCs generate the angular sizes of the BLR. Error bars for all data points reflect 1σ uncertainties.



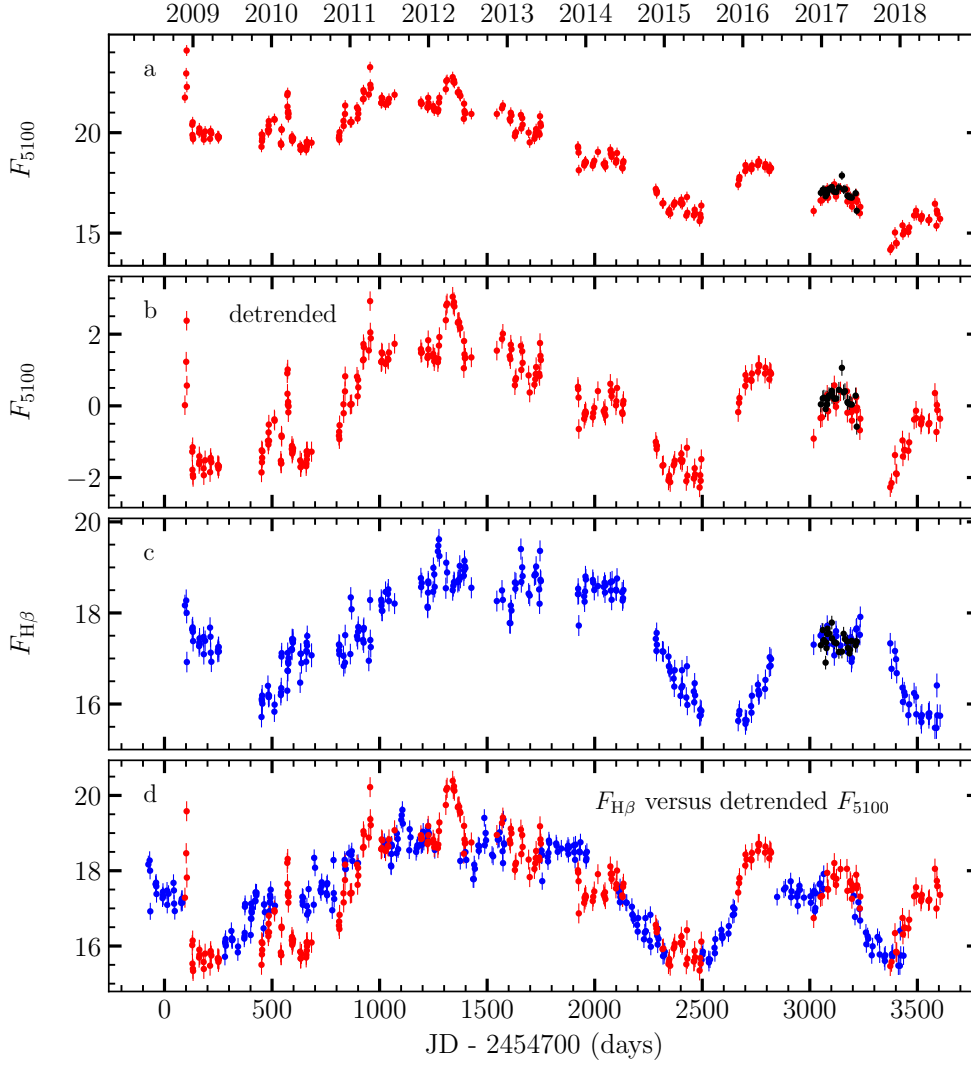
Supple-

mentary Figure 3. Corner plot of the BLR parameters and angular distances. Probability density distributions and contours of parameters are from the joint fittings of differential phase curves and $H\beta$ reverberation data. The best values of parameters are given on the tops of panels. Error bars are quoted at the 1σ level, which are given by each parameter's distributions. The dashed lines in the one-dimensional distributions are the 16%, 50% and 84% quantiles, and contours are at 1σ , 1.5σ and 2σ , respectively.



Supple-

mentary Figure 4. The *Fermi* γ -ray light curve and comparison with *V*-band observed for 10 yrs. ASAS-SN: All-Sky Automated Survey for Supernovae (see <http://www.astronomy.ohio-state.edu/~assassin/index.shtml>). Error bars for all data points reflect 1σ uncertainties. The different colors of data points in panel b indicates different sources of *V* magnitude data, as shown in the lower left corner of the panel.



Supple-

mentary Figure 5. The light curves of continuum and $H\beta$ since 2009. Panel *a*: 5100\AA (in units of $10^{-15} \text{ erg s}^{-1} \text{ cm}^{-2} \text{\AA}^{-1}$), *b*: de-trended 5100\AA , *c*: $H\beta$, and *d* $H\beta$ versus de-trended 5100\AA . In panel *d*, the $H\beta$ shifted light curve is multiplied by a scaling factor for a simple comparison. The $H\beta$ line between 2009-2012 has poor response to the varying continuum. Error bars for all data points reflect 1σ uncertainties. Red data points are light curves of continuum, while blues ones are those of $H\beta$. The black points in panels (*a*)-(*c*) are obtained from the Lijiang 2.4m telescope after inter-calibrations.

Supplementary Table 1
Targets of Future SARM Observations

No.	Name	R.A.	Declinations	z	K	V	$\log L_{5100}$ (ergs s ⁻¹)	R_{BLR} (ltc)	ξ_{BLR} (μas)	Ref.
1.	PG 0003+199/Mrk 335 [‡]	00h06m19.52s	+20d12m10.5s	0.026	10.54	14.33	43.72	10.6 - 16.8	16.6 - 26.3	R_1
2.	PG 0007+106/III Zw 2 [†]	00h10m31.01s	+10d58m29.5s	0.089	11.72	15.47	44.37	12.6	6.1	R_2
3.	PG 0050+124/I Zw 1 [‡]	00h53m34.94s	+12d41m36.2s	0.059	10.31	14.04	44.57	37.2	26.5	R_3
4.	Fairall 9	01h23m45.78s	-58d48m20.8s	0.047	10.95	13.77	44.48	17.4	15.3	R_4
5.	Mrk 1018	02h06m15.99s	-00d17m29.2s	0.042	11.33	14.31	44.17	41.3	40.1	
6.	Mrk 590/NGC 863*	02h14m33.56s	-00d46m00.1s	0.026	10.40	15.68	43.20	14.0 - 29.2	21.4 - 44.7	R_5
7.	Mrk 1044 [‡]	02h30m05.52s	-08d59m53.3s	0.016	10.81	13.94	43.49	4.8	11.6	R_6
8.	Mrk 1048/NGC 985 [†]	02h34m37.77s	-08d47m15.4s	0.043	10.84	14.02	44.30	48.6	46.4	
9.	HE 0343-3943	03h45m12.53s	-39d34m29.3s	0.043	11.13	14.64	44.04	35.5	34.2	
10.	2MASS J04145265-0755396	04h14m52.67s	-07d55m39.9s	0.038	10.89	14.75	43.90	29.7	31.9	
11.	3C 120 [†]	04h33m11.10s	+05d21m15.6s	0.033	10.51	14.15	44.01	20.2 - 38.1	24.9 - 47.0	R_7
12.	Mrk 618	04h36m22.24s	-10d22m33.8s	0.036	10.90	14.10	44.10	37.9	43.5	
13.	Ark 120/Mrk 1095 [†]	05h16m11.42s	-00d08m59.4s	0.033	10.14	14.59	43.83	16.2 - 70.0	20.2 - 87.1	R_8
14.	MCG -02-14-009	05h16m21.18s	-10d33m41.4s	0.028	11.13	15.50	43.34	15.0	21.3	
15.	2MASX J05580206-3820043	05h58m02.00s	-38d20m04.7s	0.034	10.00	14.80	43.77	25.5	30.7	
16.	2MASS J06235520+0018433	06h23m55.18s	+00d18m42.9s	0.094	11.10	15.75	44.31	49.1	22.9	
17.	NGC 2617	08h35m38.79s	-04d05m17.6s	0.014	11.65	14.00	43.33	14.9	41.6	
18.	Mrk 704 [†]	09h18m26.01s	+16d18m19.2s	0.029	10.68	14.13	43.91	30.3	42.0	R_9
19.	PG 0923+129/Mrk 705	09h26m03.29s	+12d44m03.6s	0.029	11.16	14.24	43.87	28.6	39.7	
20.	Mrk 1239	09h52m19.10s	-01d36m43.5s	0.020	9.69	14.27	43.52	18.7	37.6	
21.	NGC 3227 [†]	10h23m30.58s	+19d51m54.2s	0.004	9.73	12.48	42.81	3.8	38.2	R_{10}
22.	HE 1029-1401 [†]	10h31m54.30s	-14d16m51.0s	0.086	11.14	14.08	44.89	100.6	50.8	
23.	ESO 265- G 023	11h20m48.01s	-43d15m50.4s	0.057	11.49	14.65	44.29	47.8	35.4	
24.	PG 1126-041/Mrk 1298 [‡]	11h29m16.66s	-04d24m07.6s	0.062	11.11	14.33	44.50	61.9	42.1	
25.	NGC 3783	11h39m01.76s	-37d44m19.2s	0.010	9.83	12.60	43.56	10.2	41.5	R_{11}
26.	PG 1211+143 [‡]	12h14m17.67s	+14d03m13.1s	0.081	11.29	14.62	44.62	73.3	39.1	R_{12}
27.	PG 1226+023/3C 273 [‡]	12h29m06.70s	+02d03m08.6s	0.158	9.99	12.90	45.94	146.8 - 306.8	43.7 - 91.2	R_{13}
28.	Mrk 1330/NGC 4593	12h39m39.43s	-05d20m39.3s	0.009	9.82	12.60	43.50	3.7 - 4.3	16.4 - 18.9	R_{14}
29.	ESO 323- G 077	13h06m26.13s	-40d24m52.8s	0.015	9.32	13.22	43.69	23.1	61.3	
30.	2MASX J13411287-1438407	13h41m12.90s	-14d38m40.6s	0.042	11.25	14.36	44.13	39.7	39.1	
31.	IC 4329A	13h49m19.27s	-30d18m34.0s	0.016	9.25	13.54	43.62	15.6	38.8	R_{15}
32.	ESO 511- G 030	14h19m22.42s	-26d38m41.0s	0.022	10.96	13.93	43.76	25.0	44.9	
33.	PG 1426+015/Mrk 1383	14h29m06.59s	+01d17m06.5s	0.087	11.07	14.25	44.83	93.6	46.9	
34.	PG 1501+106/Mrk 841 [†]	15h04m01.20s	+10d26m16.2s	0.036	11.39	14.24	44.06	36.3	40.8	
35.	2MASX J15115979-2119015	15h11m59.80s	-21d19m01.7s	0.045	10.92	14.76	44.03	35.0	32.4	

36.	2MASS J16461038-1124042	16h46m10.39s	-11d24m04.2s	0.074	11.07	16.20	43.91	30.2	17.4	
37.	2MASS J17050039-0132286	17h05m00.39s	-01d32m28.6s	0.030	11.09	15.12	43.55	19.4	25.9	
38.	PDS 456	17h28m19.80s	-14d15m55.9s	0.184	9.83	14.33	45.52	216.2	56.9	
39.	Fairall 51	18h44m53.98s	-62d21m53.4s	0.014	10.20	13.94	43.36	15.3	42.8	
40.	ESO 141- G 055	19h21m14.14s	-58d40m13.1s	0.037	10.64	13.70	44.29	48.2	53.2	R_{16}
41.	2MASX J19373299-0613046	19h37m33.01s	-06d13m04.8s	0.010	10.53	13.53	43.24	13.2	50.9	
42.	NGC 6814	19h42m40.64s	-10d19m24.6s	0.005	9.81	12.97	42.87	6.6	50.1	R_{17}
43.	2MASX J19490928-1034253	19h49m09.28s	-10d34m25.0s	0.024	10.22	13.93	43.82	27.0	45.3	
44.	NGC 6860	20h08m46.89s	-61d06m00.7s	0.015	10.31	13.26	43.67	22.5	60.1	
45.	2MASS J20304171-7532430	20h30m41.63s	-75d32m42.8s	0.114	11.43	15.00	44.79	88.6	34.7	
46.	MC 2031-307	20h34m31.35s	-30d37m28.8s	0.019	10.90	13.30	43.88	29.2	60.3	
47.	Mrk 509 [‡]	20h44m09.74s	-10d43m24.5s	0.034	10.19	13.54	44.29	79.6	94.4	R_{18}
48.	2MASX J21090996-0940147	21h09m09.97s	-09d40m14.7s	0.027	10.87	13.85	43.94	31.2	47.6	
49.	[HB89] 2121-179	21h24m41.64s	-17d44m46.0s	0.112	11.38	15.20	44.69	78.5	31.4	
50.	PG 2130+099/Mrk 1513 [‡]	21h32m27.81s	+10d08m19.5s	0.063	10.63	14.46	44.46	22.9	15.3	R_{19}
51.	PG 2214+139/Mrk 304	22h17m12.26s	+14d14m20.9s	0.066	11.28	14.41	44.52	63.5	40.9	
52.	MR 2251-178	22h54m05.80s	-17d34m55.0s	0.064	11.22	14.02	44.65	74.6	49.3	
53.	NGC 7469/Mrk 1514 [†]	23h03m15.62s	+08d52m26.4s	0.016	9.63	12.84	43.92	4.5 - 10.8	11.0 - 26.4	R_{20}

*NGC 863 has another name of Mrk 590, which is known as a changing-look AGN, and recently it begins to activate again. It would be interesting to measure the BLR history from type I to type II.

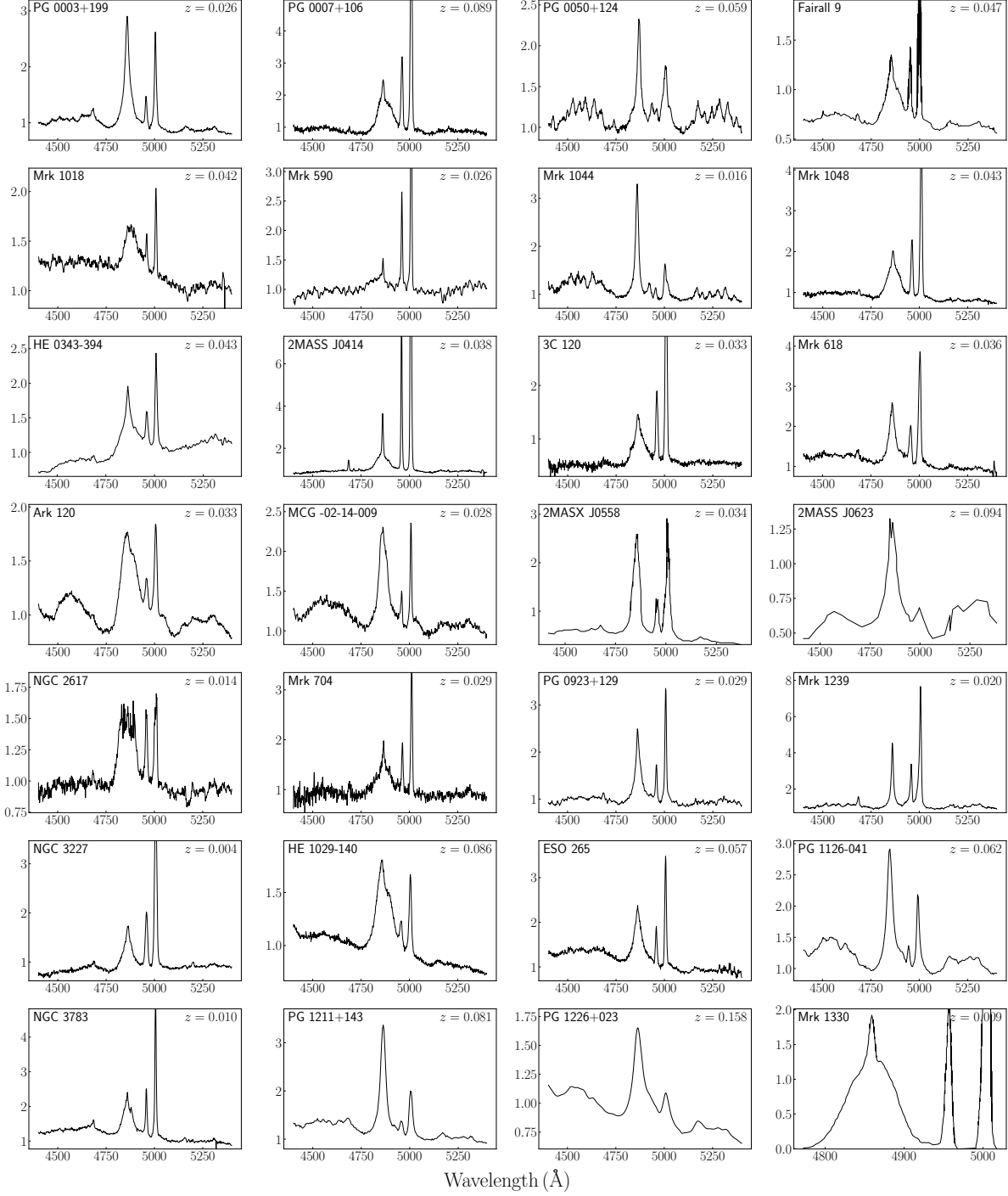
Targets marked with [†] are being conducted by the MAHA project, and with [‡] are being conducted by the SEAMBH project of the Lijiang and the Carlo Alto (CAHA) telescopes.

V -band magnitudes of most targets are given by ASAS-SN Photometry Database⁷, except: PG 0003+199 (Ref.⁸); Mrk1018 (Ref.⁹); Mrk590, Ark120 (Ref.¹⁰); MCG -02-14-009, NGC 2617, MC 2031-307 (Ref.³). K -band magnitudes of all targets are taken from 2MASS measurements¹¹. Most of them are measured using $4''$ aperture, except Mrk 1048 and NGC 6814 using $14.0'' \times 14.0''$ aperture.

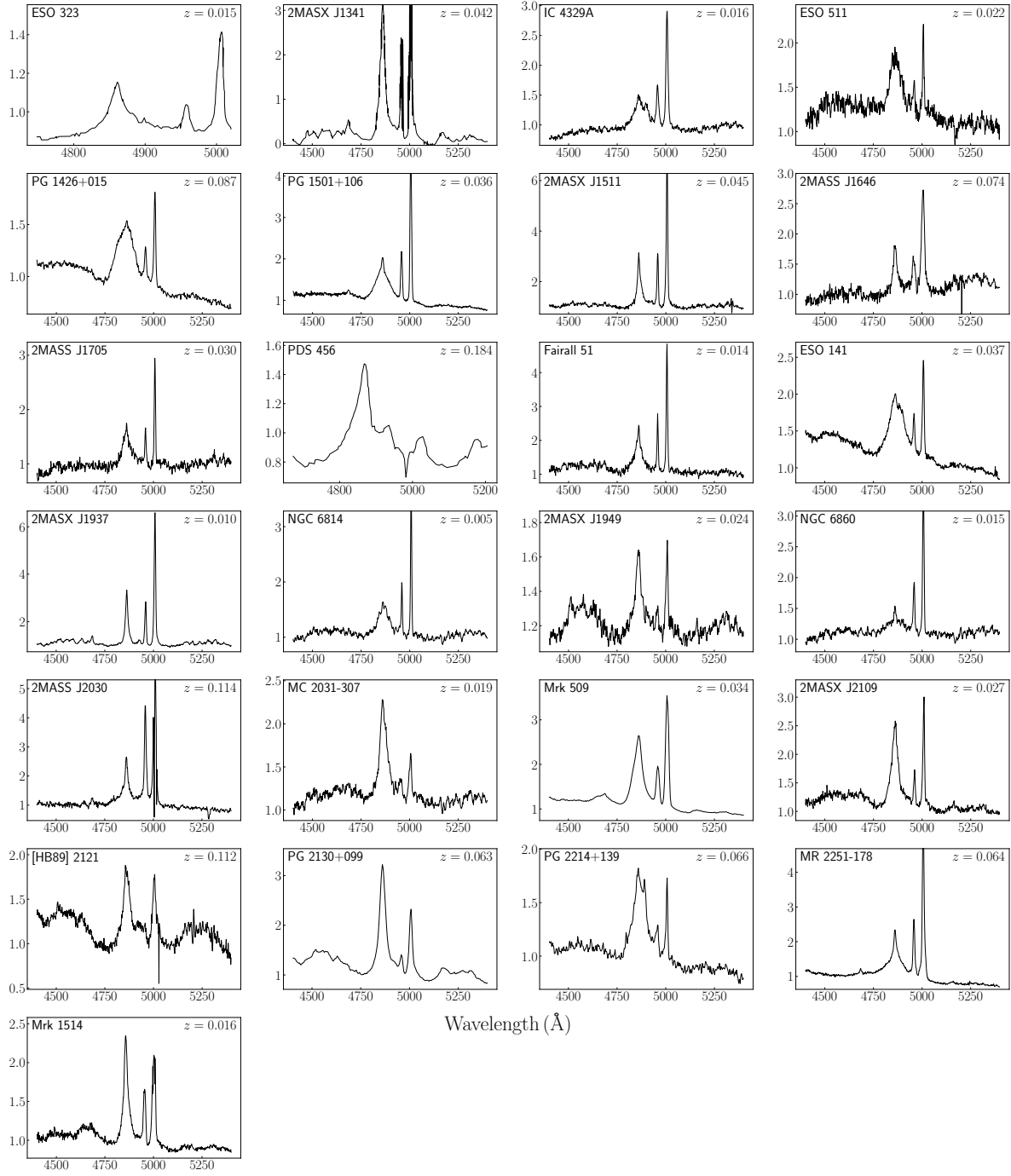
L_{5100} (in units of ergs s^{-1}) is estimated using V -band magnitude and luminosity distances, assuming a composite quasar spectra from the SDSS¹² for all objects.

For those mapped targets, R_{BLR} is from measured time lags or the minimum and maximum lags (if there are multiple campaigns). Mrk 704 and ESO 141- G 055 were mapped, but failed to measure reliable lags due to the poor quality of the data. For targets without mapping campaigns, lags are estimated by the $R - L$ relation⁴⁰ for AGN. Angular size for all target are calculated through $\xi_{\text{BLR}} = R_{\text{BLR}}/D_A$.

References of mapped AGNs: R_1 : Ref.¹³⁻¹⁶; R_2 : Ref.¹⁵; R_3 : Ref.¹⁷; R_4 : Ref.^{18,19}; R_5 : Ref.^{13,14}; R_6 : Ref.²⁰; R_7 : Ref.^{13-15,21,22}; R_8 : Ref.^{13,14,18,22,23}; R_9 : Ref.¹³; R_{10} : Ref.²⁴; R_{11} : Ref.²⁵; R_{12} : Ref.^{14,26}; R_{13} : Ref.^{26,27}; R_{14} : Ref.^{28,29}; R_{15} : Ref.¹⁸; R_{16} : Ref.¹⁸; R_{17} : Ref.³⁰; R_{18} : Ref.^{13,14}; R_{19} : Ref.¹⁵; R_{20} : Ref.^{14,31,32};



Supplementary Figure 6. Spectra of all selected targets of the SARM projects in rest frame. All the spectra are from publications (see references). Spectral fluxes are in units of $\text{ergs s}^{-1} \text{\AA}^{-1}$ but scaled by arbitrary factors for convenience. Ref. Of spectra: object No. 1 is from Ref.¹⁶; No. 2, 8, 10, 12, 17, 18 and 30 from the MAHA project;



Supplementary Figure 6 continued. No. 3 from Ref.¹⁹; No. 6 from Ref.²⁰; No. 4, 5, 7, 9, 11, 13, 16, 19, 21, 27, 28, 31-33, 35-42, 44, 45 and 48 from Ref.³³; No. 14 and 26 from Ref.³⁴; No. 15, 20, 29, 46, 47 and 49 from Ref.³⁵; No. 22 and 43 from the CAHA project; No. 23 from Ref.²⁷; No. 24 from Ref.³⁶; No. 25 from Ref.³⁷; No. 34 from Ref.³⁸.

1. Croom, S. M. et al. The 2dF QSO redshift survey - XII. The spectroscopic catalogue and luminosity function. *Mon. Not. R. Astron. Soc.* **349**, 1397-1418 (2004).
2. Masci, F. J. et al. The southern 2MASS AGNs survey: spectroscopic follow-up with six degree field. *Pub. Astron. Soc. Australia* **27**, 302-320 (2010).
3. Veron-Cetty, M.-P. and Veron, P. A catalog of quasars and active galactic nuclei (13th Edition). *Astron. Astrophys.* **518**, A10-A17 (2010).
4. Wisotzki, L. et al. The Hamburg/ESO survey for bright QSOs. III. A large flux-limited sample of QSOs. *Astron. Astrophys.* **358**, 77-87 (2000).
5. Pâris, I. et al. The Sloan Digital Sky Survey Quasar Catalog: fourteenth data release. *Astron. Astrophys.* **613**, A51 (2018).
6. Bentz, M. C. et al. The low-luminosity end of the radius-luminosity relationship for active galactic nuclei. *Astrophys. J.* **767**, 149 (2013).
7. Kochanek, C. S. et al. The All-Sky Automated Survey for Supernovae (ASAS-SN) light curve server v1.0. *Pub. Astron. Soc. Pac.* **129**, 104502 (2017).
8. Haas, M. et al. Photometric AGN reverberation mapping - an efficient tool for BLR sizes, black hole masses, and host-subtracted AGN luminosities. *Astron. Astrophys.* **535**, A73 (2011).
9. de Vaucouleurs, A., & Longo, G. Catalogue of visual and infrared photometry of galaxies from 0.5 micrometer to 10 micrometer (1961-1985). University of Texas Monographs in Astronomy (1988).

10. Bentz, M. C., Peterson, B. M., Pogge, R. W., Vestergaard, M. The black hole mass-bulge luminosity relationship for active galactic nuclei from reverberation mapping and Hubble Space Telescope Imaging. *Astrophys. J. Letters* **694**, L166-L170 (2009).
11. Skrutskie, M. F. et al. The Two Micron All Sky Survey (2MASS). *Astron. J.* **131**, 1163-1183 (2006).
12. Vanden Berk, D. E. et al. Composite quasar spectra from the Sloan Digital Sky Survey. *Astron. J.* **122**, 549-564 (2001).
13. Peterson, B. M., Wanders, I., Bertram, R., Hunley, J. F., Pogge, R. W., Wagner, R. M. Optical continuum and emission-line variability of Seyfert 1 galaxies. *Astrophys. J.* **501**, 82-93 (1998).
14. Peterson, B. M. et al. Central masses and broad-line region sizes of active galactic nuclei. II. A homogeneous analysis of a large reverberation-mapping database. *Astrophys. J.* **613**, 682-699 (2004).
15. Grier, C. J. et al. Reverberation mapping results for five Seyfert 1 galaxies. *Astrophys. J.* **755**, 60-75 (2012).
16. Du, P. et al. Supermassive black holes with high accretion rates in AGNs. I. First results from a new reverberation mapping campaign. *Astrophys. J.* **782**, 45 (2014).
17. Huang, Y.-K. et al. Reverberation mapping of the narrow-line Seyfert 1 galaxy I Zwicky 1: black hole mass. *Astrophys. J.* **876**, 102 (2019).

18. Winge, C., Peterson, B. M., Pastoriza, M. G., Storchi-Bergmann, T. Spectroscopic monitoring of AGNs from CTIO. II. IC 4329A, ESO 141-G55, Arakelian 120, and Fairall 9. *Astrophys. J.* **469**, 648-661 (1996).
19. Santos-Lleó, M. et al. Steps toward determination of the size and structure of the broad-line region in active galactic nuclei. X. Variability of Fairall 9 from optical data. *Astrophys. J. Supp.* **112**, 271-283 (1997).
20. Wang, J.-M. et al. Supermassive black holes with high accretion rates in active galactic nuclei. II. The most luminous standard candles in the Universe. *Astrophys. J.* **793**, 108 (2014).
21. Kollatschny, W., Ulbrich, K., Zetzl, M., Kaspi, S., & Haas, M. Broad-line region structure and kinematics in the radio galaxy 3C 120. *Astron. Astrophys.* **566**, A106 (2014).
22. Du, P. et al. Monitoring AGNs with $H\beta$ Asymmetry. I. First results: velocity-resolved reverberation mapping. *Astrophys. J.* **869**, 142 (2018).
23. Doroshenko, V. T., Sergeev, S. G., & Pronik, V. I. The Seyfert 1 galaxy Ark 120. Spectral variability in 1992-2005. *Astron. Rep.* **52**, 442-462 (2008).
24. Denney, K. D. et al. Reverberation mapping measurements of black hole masses in six local Seyfert galaxies. *Astrophys. J.* **721**, 715-737 (2010).
25. Stirpe, G. M. et al. Steps toward determination of the size and structure of the broad-line region in active galactic nuclei. VI. Variability of NGC 3783 from ground-based data. *Astrophys. J.* **425**, 609-621 (1994).

26. Kaspi, S., Smith, P. S., Netzer, H., Maoz, D., Jannuzi, B. T., Giveon, U. Reverberation measurements for 17 quasars and the size-mass-luminosity relations in active galactic nuclei. *Astrophys. J.* **533**, 631-649 (2000).
27. Zhang, Z.-X. et al. Kinematics of the broad-line region of 3C 273 from a 10 yr reverberation mapping campaign. *Astrophys. J.* **876**, 49 (2019).
28. Denney, K. D. et al. The mass of the black hole in the Seyfert 1 galaxy NGC 4593 from reverberation mapping. *Astrophys. J.* **653**, 152-158 (2006).
29. Barth, A. J. et al. The Lick AGN monitoring project 2011: Fe II reverberation from the outer broad-line region. *Astrophys. J.* **769**, 128 (2013).
30. Bentz, M. C. et al. The Lick AGN monitoring project: broad-line region radii and black hole masses from reverberation mapping of $H\beta$. *Astrophys. J.* **705**, 199-217 (2009).
31. Collier, S. J. et al. Steps toward determination of the size and structure of the broad-line region in active galactic nuclei. XIV. Intensive optical spectrophotometric observations of NGC 7469. *Astrophys. J.* **500**, 162-172 (1998).
32. Peterson, B. M. et al. Reverberation mapping of the Seyfert 1 galaxy NGC 7469. *Astrophys. J.* **795**, 149 (2014).
33. Jones, D. H. et al. The 6dF Galaxy Survey: final redshift release (DR3) and southern large-scale structures. *Mon. Not. R. Astron. Soc.* **399**, 683-698 (2009).

- 34. Marziani, P. et al. An optical spectroscopic atlas of low-redshift active galactic nuclei. *Astrophys. J. Supp.* **145**, 199-211 (2003).
- 35. Boroson, T. A., & Green, R. F. The emission-line properties of low-redshift quasi-stellar objects. *Astrophys. J. Supp.* **80**, 109-135 (1992).
- 36. Williams, P. R. et al. The Lick AGN Monitoring Project 2011: Dynamical modeling of the broad-line region. *Astrophys. J.* **866**, 75 (2018).
- 37. Thomas, A. D. et al. Probing the physics of narrow-line regions in active galaxies. IV. Full data release of the Siding Spring Southern Seyfert Spectroscopic Snapshot Survey (S7). *Astrophys. J. Supp.* **232**, 11 (2017).
- 38. Simpson, C., Ward, M., O'Brien, P., Reeves, J. Optical and infrared observations of the luminous quasar PDS 456: a radio-quiet analogue of 3C 273? *Mon. Not. R. Astron. Soc.* **303**, L23-L28 (1999).